Phenotypic and genetic associations of quantitative magnetic susceptibility in UK Biobank brain imaging

Chaoyue Wang[1]*, Aurea B. Martins-Bach[1], Fidel Alfaro-Almagro[1], Gwenaëlle Douaud [1], Johannes C. Klein[1,2], Alberto Llera[3], Cristiana Fiscone[4,5], Richard Bowtell[4], Lloyd T. Elliott[6], Stephen M. Smith[1], Benjamin C. Tendler[1,†] and Karla L. Miller[1,†]

1. Wellcome Centre for Integrative Neuroimaging, FMRIB, Nuffield Department of Clinical Neurosciences, University of Oxford

2. Oxford Parkinson's Disease Centre, University of Oxford, Oxford, UK

3. Donders Institute for Brain, Cognition and Behaviour, Centre for Cognitive Neuroimaging, Nijmegen, Netherlands

4. Sir Peter Mansfield Imaging Centre, School of Physics and Astronomy, University of Nottingham, Nottingham, United Kingdom

5. Department of Biomedical and Neuromotor Sciences, University of Bologna, Bologna, Italy

6. Department of Statistics and Actuarial Science, Simon Fraser University, Vancouver, BC, Canada

† Equal contribution

*Address for Correspondence:
Chaoyue Wang
Wellcome Centre for Integrative Neuroimaging (WIN), FMRIB
John Radcliffe Hospital, Headington, Oxford
OX3 9DU, UK
Tel: +44 (0) 1865 611450
Email: chaoyue.wang@ndcn.ox.ac.uk

Abstract

A key aim of epidemiological neuroscience studies is the identification of novel markers to assess brain health and evaluate the efficacy of therapeutic interventions. A broad range of tissue constituents associated with healthy brain functions and diseases (e.g., iron, myelin and calcium) are characterised by unique magnetic properties, motivating the development of measurements sensitive to these effects. Quantitative susceptibility mapping (QSM) is an emerging MRI technique which enables in vivo quantification of tissue magnetic susceptibility, providing the opportunity to identify such markers. In this study, we developed a robust QSM modelling pipeline and evaluated the potential of QSM in a cohort of 35,885 subjects (ages 45-82), alongside extensive genetic and phenotypic associations as part of UK Biobank. Our analysis identified a rich set of distinctive phenotypic and genetic associations with QSM. This included phenotypic associations with body iron, diet, alcohol and diseases, and genetic associations related to a broad range of biological functions including iron, calcium homeostasis, myelination, extracellular matrix. Importantly, we found that QSM and T2* have unique patterns of associations, demonstrating the added value in including QSM IDPs in the UK Biobank brain imaging resource, with considerable promise to identify novel in vivo brain health markers.

Introduction

Magnetic resonance imaging (MRI) is a powerful, non-invasive technology for studying the brain. Although MRI visualises anatomical structures on the scale of millimetres [1], it is nevertheless sensitive to cellular phenomena at the microscopic scale. In particular, susceptibility-weighted MRI (swMRI) data is sensitive to brain iron, myelin and calcium content via their shifted magnetic susceptibility compared to tissue water [2–4]. Recent advances in image processing have enabled swMRI data to be transformed into a quantitative map of magnetic susceptibility, denoted as χ. Due to its quantitative relationship to these disease-relevant tissue properties, quantitative susceptibility mapping (QSM) has the potential to play a pivotal role in the study of neurological and psychiatric disorders [5–8].

The impact of QSM to date has partially limited by the size and scope of available datasets, typically consisting of tens or hundreds of subjects [9]. The dominant strategy in these studies has been to use clinically-defined cohorts to maximize statistical power. This approach has been effective in identifying markers relating to pathological changes in χ. A more challenging aim is to determine whether QSM might provide predictive markers early in disease, which could provide crucial information for therapeutic development and monitoring. In general, this requires imaging at the pre-symptomatic stage when it is often difficult or impossible to design small cohorts that are likely to develop a given condition.

UK Biobank is a prospective epidemiological cohort of 500,000 participants (40-69 years of age at baseline recruitment) who have been deeply phenotyped and genotyped. The study aims to scan 100,000 participants with a multi-organ MRI protocol [10,11]. Crucially, these subjects have all been scanned when they are largely healthy, and UK Biobank includes long-term access to participants' health records via the UK National Health Service.

The UK Biobank brain imaging protocol includes swMRI, which creates unique opportunities to investigate QSM in previously unexplored territory, including as a marker for early disease. Importantly, the two-echo swMRI protocol was configured to output both magnitude data, which can be used to quantify the transverse relaxation time T2*, and phase data, which can provide χ estimates via QSM. For most brain imaging modalities, UK Biobank was able to build on the analysis pipelines developed by the Human Connectome Project [12,13]; however, no such pipeline existed for swMRI data. The straightforward nature of T2* calculations meant that these measures were included in the original UK Biobank image processing pipeline. In comparison, QSM requires sophisticated, multi-step processing of phase data to produce accurate and reproducible χ maps [14–16], and as such QSM was not included in the original UK Biobank processing pipeline.

We present the first QSM results from UK Biobank, based on the current release of data from 35,885 subjects, with 1,447 subjects also having had repeat imaging after a 2-year interval. We conducted a comprehensive evaluation of established algorithms for each processing step, resulting in a fully-automated and optimised QSM analysis pipeline. The output χ maps were used to calculate imaging-derived phenotypes (IDPs) relating to χ in a range of subcortical grey matter structures and white matter hyperintensity lesions. We present associations between these IDPs and a broad range of non-imaging phenotypes, including diet, blood assays and health outcomes. We also present the first genome-wide association studies (GWAS) using QSM IDPs, identifying relationships with genes with known relevance to iron, myelin and other sources of χ shift in brain tissue, as well as other less readily interpretable associations. These results demonstrate the richness of information in QSM data and the potential to discover

subtle relationships. Importantly, we found that QSM and T2* have distinct patterns of associations, demonstrating the added value in including QSM IDPs in the UK Biobank brain imaging resource. QSM processing is being incorporated into the core UK Biobank brain imaging processing pipeline [12]. Spatial χ maps and IDPs will be returned to UK Biobank for inclusion in the resources available to researchers worldwide.

RESULTS

Data analyses

We conducted an extensive evaluation of existing algorithms for each processing step to establish an automated QSM pipeline, as detailed in Supplementary Material (Section 1.1). Here, we describe the final pipeline as illustrated in **Figure 1a**. The phase data of individual channels is first combined following the MCPC-3D-S approach [17]. Channel-combined phase data from each echo are subsequently unwrapped using a Laplacian-based algorithm [18], and averaged following the weighting procedure described in Wu et al. [19]. The resulting phase images are filtered using the V-SHARP algorithm [20] to remove background fields. Finally, χ maps are calculated using the iLSQR algorithm [21] and referenced to the χ value of cerebrospinal fluid in the lateral ventricles. A QSM population average template (**Fig. 1b**) was produced by averaging χ maps aligned to MNI space from all 35,273 subjects with usable swMRI data.

Median T2* values in 14 major subcortical grey matter regions (thalamus, caudate, putamen, pallidum, hippocampus, amygdala and accumbens, both left and right) have already been produced as T2*-based IDPs in the current UK Biobank data release. We produced equivalent QSM-based IDPs, calculated as median χ values in these 14 subcortical regions (using the same masks for subcortical regions). We additionally generated 6 new IDPs for swMRI data: (1) median χ (and, separately, T2*) in the substantia nigra (left and right), and (2) difference in χ (and T2*) between white matter hyperintensity (WMH) lesions and normal-appearing white matter (identified from separate T2-weighted FLAIR images) [12].

QSM and T2* estimates reflect different statistical properties of χ within a voxel. T2* is driven by cellular compartments with a χ offset (for example, the myelin sheath or iron packaged by ferritin), corresponding to heterogeneously distributed χ that broadens the distribution of frequencies within a voxel and leads to a T2* decrease [22]. In contrast, QSM provides a quantitative estimate of the bulk (mean) χ in an imaging voxel, regardless of how χ is distributed across the voxel [14]. One fundamental difference between QSM- and T2*-derived measurements is that paramagnetic substances (such as iron) and diamagnetic substances (such as myelin and calcium) have opposite effects on QSM (opposite sign of estimated χ), but the same effect on T2* (reducing T2*) [23].

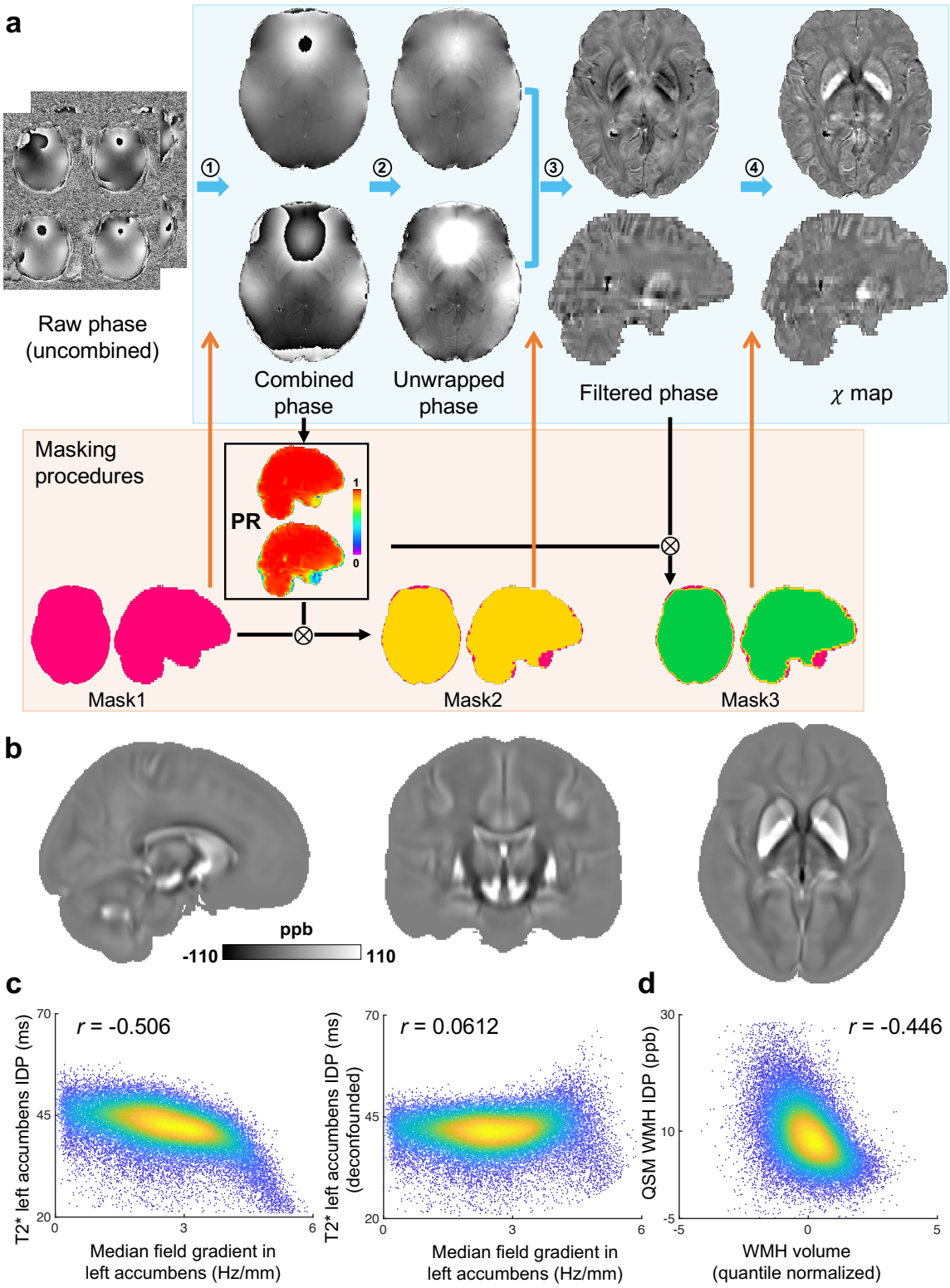

Figure 1 (a) Visualization of QSM processing pipeline for UKB swMRI data. Blue arrows indicate the main processing steps. Step 1: Channel combination using MCPC-3D-S. Step 2: Phase unwrapping using a Laplacian-based algorithm. Step 3: Background field removal using V-SHARP. Step 4: Dipole inversion using iLSQR. Black arrows indicate the evolution of brain masks. Orange arrows indicate the brain masks applied for each step. The masks are refined using a 'phase reliability' (effectively, 1/local phase variance) map (PR, black box). First, the initial brain mask (mask1, pink) provided by UKB is used for channel combination. Second, mask1 is updated by thresholding the phase reliability map to exclude voxels in the vicinity of sinus cavities (mask2, yellow) and is applied to V-SHARP. Finally,

the output mask from V-SHARP is updated by further thresholding the phase reliability map, the resulting mask (mask3, green) is applied to the dipole inversion step. Details about the pipeline are provided in the (Supplementary Material Section 1.1). **(b)** QSM atlas generated by averaging χ maps (non-linearly registered to MNI space) from all available subjects. **(c)** Example association between T2* left accumbens IDP and median field gradient measured in the left accumbens before (r=-0.506) and after (r=0.0612) deconfounding based on physical models (details in Supplementary Information). **(d)** Association between QSM WMH IDP and WMH volume IDP (*r*=-0.446).

Estimation of biologically-meaningful T2* reflecting cellular compartments is confounded by the presence of macroscopic field gradients that are induced by air/tissue interfaces or poor magnetic field shim quality [24]. These field gradients are particularly acute when acquiring large voxels, such as the relatively thick imaging slices in the UK Biobank swMRI protocol [24]. In large-cohort epidemiological studies, this could lead to spurious correlations that are driven by subject-wise variations in field homogeneity (for example, geometry of the nasal cavities, or other anatomical structures outside the brain) rather than cellular phenomena (**Figure 1c**). In this study, an additional set of confounding variables that account for the presence of macroscopic field gradients were derived from physical models relating these gradients to a reduction in T2* and were removed from each T2*-based IDP before conducting association analyses (calculated as a regression from $T2^{*-1}$, details provided in Supplementary Material, Section 2). As expected, these confounds had very low correlation with QSM IDPs (**Supplementary Fig. S18**) and were thus not included in QSM-related analyses.

In reproducibility analysis using the two-timepoint data from 1,447 subjects (with the assumption that negligible changes in χ/T2* occurred during the two timepoints), subcortical QSM IDPs generally showed higher reproducibility (cross-scan correlation r) compared with corresponding T2* IDPs (**Supplementary Fig. S13**), particularly in the caudate, putamen, pallidum and substantia nigra ($0.8 < r < 0.9$ for QSM and $0.6 < r < 0.8$ for T2*).

Associations between IDPs and non-imaging phenotypes

We carried out univariate (pairwise) association analyses between 17,485 UK Biobank non-imaging phenotypes and QSM/T2* IDPs. We observed strong correlations between QSM/T2* WMH IDPs and the WMH volume IDP in the current UK Biobank data release (**Fig. 1d**): to account for potential partial volume effect, association analyses with WMH IDPs were conducted twice, with and without regressing out the WMH volume IDP (resulting in a total of 18 sets of correlations with non-imaging phenotypes for QSM or T2* IDPs). For the remainder of this manuscript, we refer to all non-imaging phenotypes as "phenotypes", as distinct from IDPs. These phenotypes have been grouped into 17 categories including early life factors (e.g., birth weight, maternal smoking), lifestyle factors (e.g., diet, alcohol and tobacco consumption), physical/body measures (e.g., BMI, bone density and blood assays), cognitive test scores (e.g., numeric memory), health outcomes (e.g., clinical diagnosis – ICD10 and operative procedures – OPCS4) and mental health variables (e.g., bipolar and major depression status). After Bonferroni multiple comparison correction, 327 phenotypes showed significant associations with QSM IDPs. In this case, with 297,245 (17,485 x 18) calculated correlations, Bonferroni corresponds to $P < 1.59 \times 10^{-7}$. We follow the convention for Manhattan plots and display results using $-\log_{10}(P)$, with the Bonferroni threshold being a significance threshold of $-\log_{10}(P) > 6.80$ (**Fig. 2**). The full list of significant associations is provided in **Supplementary Table 1**.

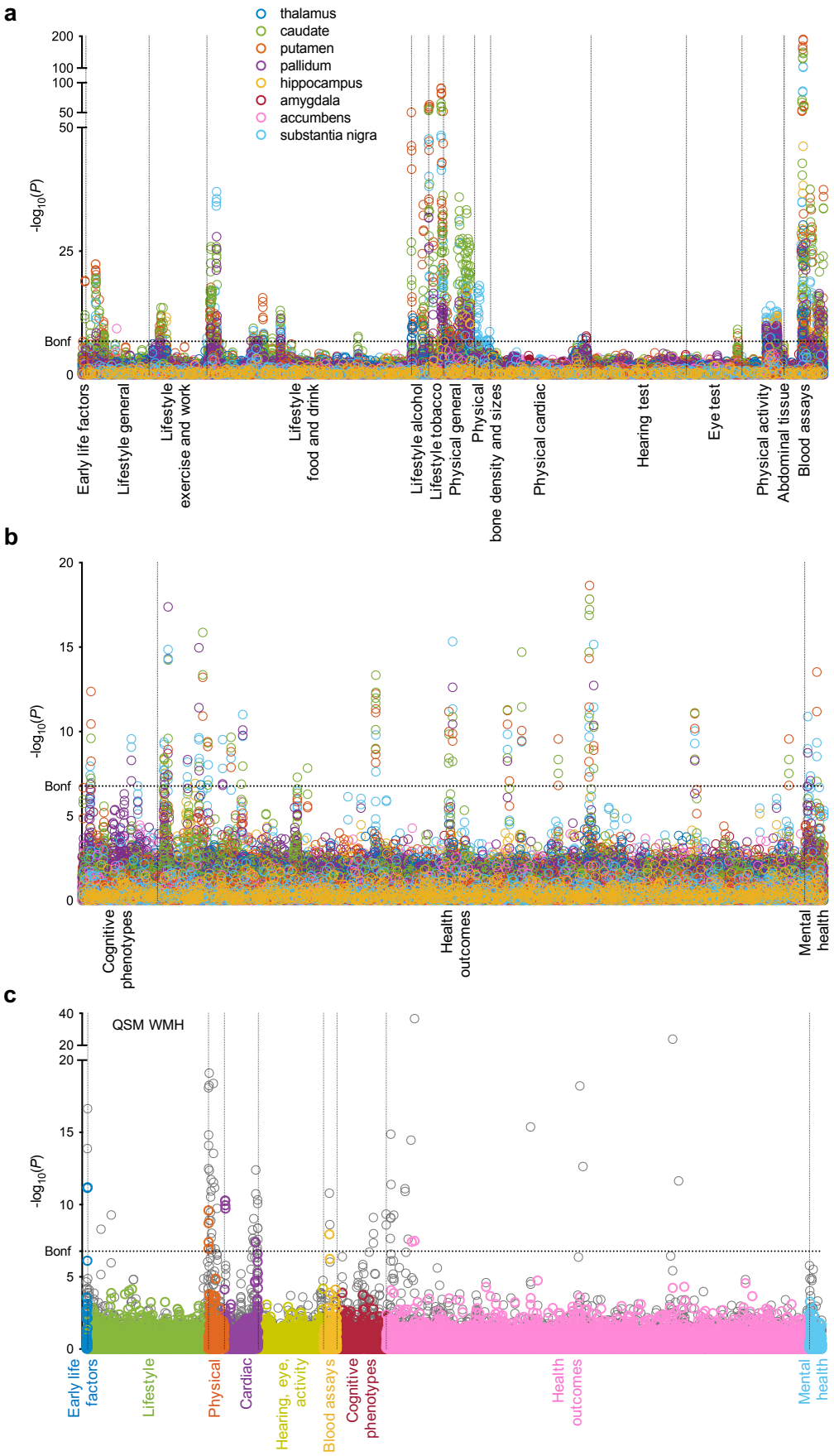

Figure 2 Visualization of 297,245 univariate cross-subject association tests between QSM IDPs and 17,485 phenotypes in UK Biobank. **(a)** Manhattan plot showing associations between 16 subcortical

QSM IDPs and phenotypes in 14 categories including lifestyle, physical, and blood measures. **(b)** Manhattan plot showing associations between 16 subcortical QSM IDPs and phenotypes in 3 categories including cognition, health outcomes and mental health measures. **(c)** Manhattan plot showing associations between QSM WMH IDP and all phenotypes (separated into 9 major categories). Shown behind (grey) are the associations without regressing out WMH volume.

For each phenotype category, the strength of associations with subcortical QSM and T2* IDPs was compared to identify the consistent as well as the complementary results for these two quantitative measures (details are provided in Supplementary Material, section 3). We found that associations in some phenotype categories (for example, *alcohol consumption*) are more specific to QSM IDPs (**Fig. 3a, b**) whereas other categories (for example, *cardiac*) are more specific to T2* IDPs (**Fig. 3c, d**). However, the majority of the categories showed a mixed pattern of findings where QSM and T2* IDPs showed both similar and distinct associations (for example, *blood assays*) (**Fig. 3e**). This overall picture agrees with the expectation that QSM and T2* measures do not trivially recapitulate the same tissue properties, but together provide rich information from a single scan.

Producing IDPs is one approach to reduce raw data into a compact and robust set of measures suitable for discovery analyses, such as the phenome-wide associations described above. However, associations with summary measures like IDPs can lose the richness of spatial information in the raw data. Interrogating associations at a voxel-wise level can provide further insight about the detailed spatial localization of associations, including identification of associations that do not respect the atlas-based regional boundaries used to generate IDPs. Voxel-wise associations between χ maps (aligned to MNI space) and phenotypes are shown in **Figure 4** for 8 representative phenotypes. Other voxel-wise association maps with selected phenotypes (for example, phenotypes that showed the strongest correlations with QSM IDPs in each category) are provided in Supplementary Material (Section 4). Each voxel-wise association map has a unique pattern of spatial associations including extended homogeneous regions, more focal associations with sub-regions, and associations with additional areas not included in the ROIs used to generate QSM IDPs.

Below, we describe associations identified between IDPs and phenotypes in more detail, focusing on associations that validate findings of previous studies, and/or associations that are more specific to QSM IDPs (given that T2* results have been published previously).

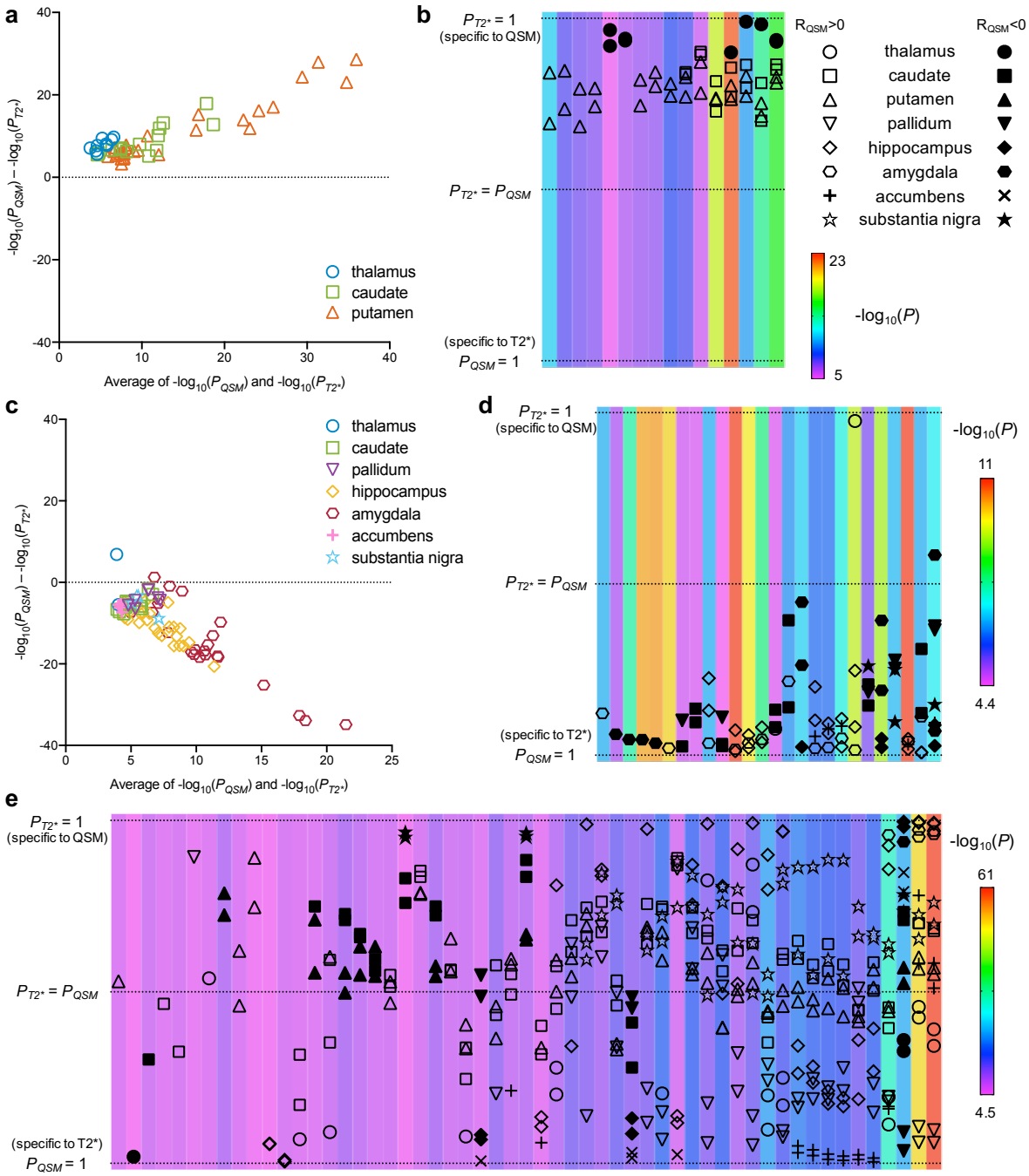

Figure 3 Example comparisons of phenotypic associations with QSM and T2* subcortical IDPs (ROI/phenotype pair is shown if either its P_{QSM} or P_{T2*} passed the Bonferroni-corrected threshold). Results are given for **(a,b)** alcohol consumption, **(c,d)** cardiac and **(e)** blood assay categories. **(a,c)** Bland-Altman plot showing comparisons of -log$_{10}P$ values between QSM versus T2* associations for the (a) alcohol consumption and (c) cardiac categories. **(b,d,e)** Transformed Bland-Altman plot that aims to emphasise whether a given association is specific to QSM, T2*, or common to both. Each column represents one unique phenotype in Bland-Altman plots, and includes all IDPs that pass significance threshold. The vertical-axis is given by the angle of each point in a Bland-Altman plot with respect to the y=0 line. Hence, datapoints at the top (or bottom) of the plot represent an association that is highly specific to QSM (or T2*), and datapoints in the middle are phenotypes that associate with both QSM and T2* in a given brain region. Unlike the Bland-Altman plot, this visualisation emphasises the modality specificity over the strength of correlation. For example, it is more apparent in (b) compared to (a) that thalamus-alcohol associations are highly specific to QSM. The background colour of each column represents the average -log$_{10}P$ for significant associations with that phenotype.

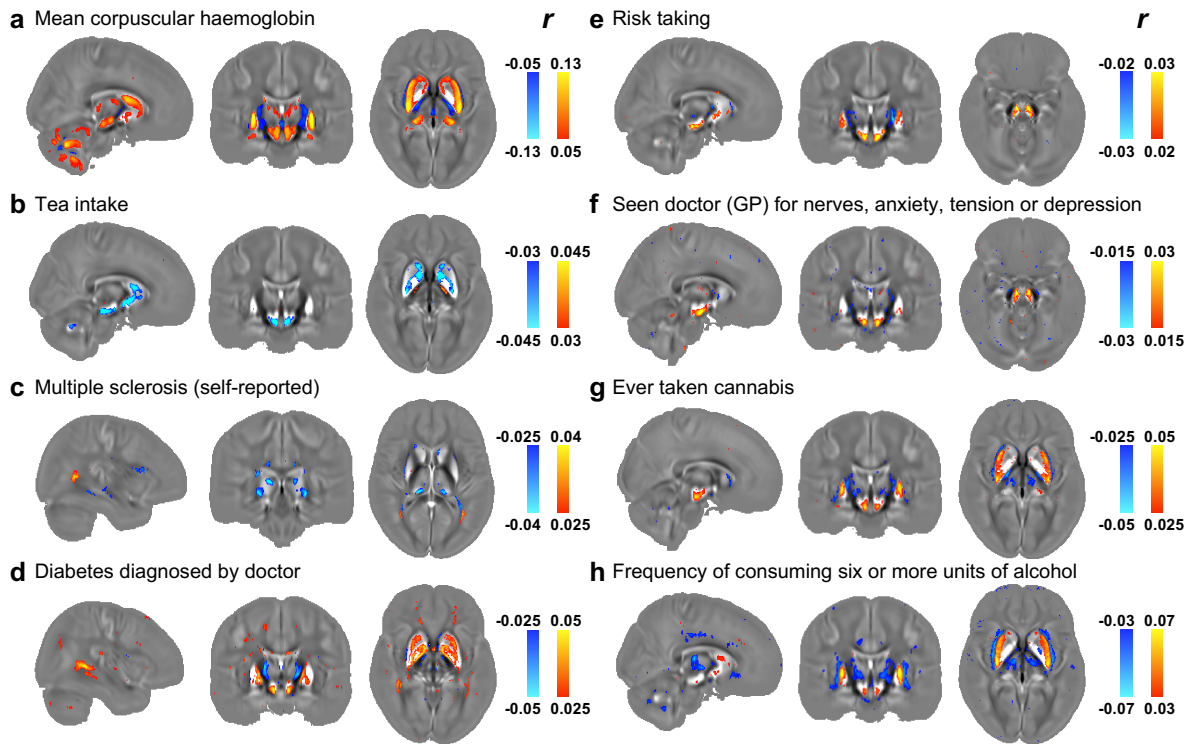

Figure 4 Voxel-wise correlation maps of 8 example phenotypes with χ maps aligned in MNI space. In associations with QSM subcortical IDPs, **(a)** *mean corpuscular haemoglobin* was associated with all subcortical QSM IDPs; **(b)** *tea intake* was associated with QSM IDPs in the caudate, putamen, pallidum and substantia nigra; **(c)** *multiple sclerosis (self-reported)* was only associated with QSM right thalamus IDP; **(d)** *diabetes diagnosed by doctor* was associated with QSM IDPs in the caudate, putamen, pallidum and substantia nigra; **(e)** *risk taking* was associated with QSM IDPs in the pallidum and substantia nigra; **(f)** *seen doctor (GP) for nerves, anxiety, tension or depression* was only associated with QSM right substantia nigra IDP; **(g)** *ever taken cannabis* was associated with QSM IDPs in the caudate, putamen and substantia nigra; **(h)** *frequency of consuming six or more units of alcohol* was associated with QSM IDPs in the thalamus, caudate and putamen.

Phenotypic associations with subcortical IDPs

Blood assays

In the blood assays category, 47 phenotypes were significantly associated with subcortical QSM IDPs including the strongest association among all phenotypic associations with QSM IDPs, that was found between *mean corpuscular haemoglobin* and the right putamen ($r = 0.16, P = 4.24 \times 10^{-191}$). In general, haemoglobin-related phenotypes in the blood assay category showed strong, positive correlations with all 16 subcortical QSM IDPs (**Fig. 2a** and **Supplementary Table 1**). Notably, haemoglobin-related blood measures are used clinically as a marker for a subject's iron levels [25]. In addition, iron-related disease diagnoses such as *iron deficiency anaemia* demonstrated negative correlations with subcortical QSM IDPs (**Supplementary Table 1**). The positive sign of associations with haemoglobin measures (and negative sign with iron deficiency diagnoses) agrees with the positive correlation between χ and iron concentration reported in post-mortem studies [26]. The voxel-wise map of associations with *mean corpuscular haemoglobin* (**Fig. 4a**) displayed spatially contiguous associations in the subcortical regions captured with our IDPs, but also in the red nucleus and cerebellar regions for which we have not generated IDPs. Notably, the spatial localization patterns differed across these regions, with the putamen, substantia nigra and red nucleus displaying

homogeneous correlations across the entire region, while voxels in the pallidum, hippocampus and thalamus cluster predominantly in specific sub-regions. Finally, note that all the spatial maps shown in Fig. 4 are highly symmetric (i.e., though we report above the strongest blood assay association as being in right putamen, left putamen is very similar).

Food and drink

In the food and drink category, 47 phenotypes were significantly associated with subcortical QSM IDPs. Phenotypes related to tea consumption reveal a negative correlation with χ in multiple subcortical structures (including caudate, putamen, pallidum and substantia nigra) where the strongest correlation was between *tea intake* and QSM in the left substantia nigra ($r = -0.069, P = 9.76 \times 10^{-38}$). Although no direct link between tea intake and χ measures have been described previously, polyphenols in both green and black tea have been reported as brain-permeable, natural iron chelators that have demonstrated neuroprotective effects [27,28]. The voxel-wise association map with *tea intake* (**Fig. 4b**) revealed spatially contiguous associations in sub-regions of the caudate, pallidum and substantia nigra. This spatial pattern of correlations is in line with a previous study investigating a rat model of Parkinson's disease, where oral administration of black tea extract reduced oxidative stress levels in the substantia nigra and striatum in rats with 6-hydroxydopamine lesions [27].

Health outcomes

In the health outcomes category, 40 phenotypes were significantly associated with subcortical QSM IDPs. For example, we identified an association between *multiple sclerosis* (*self-reported)* and QSM in right thalamus ($r = -0.028, P = 1.42 \times 10^{-7}$). The voxel-wise association map with *multiple sclerosis* (*self-reported)* (**Fig. 4c**) revealed spatially contiguous associations in sub-regions of both left and right thalamus and in focal white matter regions such as the optic radiation. This result agrees with previous studies of multiple sclerosis (MS) that reported reduced χ in thalamus in MS patients compared to healthy controls [7,8,29]. In addition to the large group of iron deficiency related diagnoses, another major diagnosis group, diabetes, is associated with QSM in caudate, putamen, pallidum and substantia nigra, where the strongest association is between QSM in the right pallidum and *diabetes diagnosed by doctor* ($r = 0.047, P = 4.15 \times 10^{-18}$). Voxel-wise association map with *diabetes diagnosed by doctor* (**Fig. 4d**) revealed spatially contiguous associations in caudate, putamen, pallidum and substantia nigra regions as well as in many white matter regions such as the splenium of the corpus callosum and optic radiation. Although this phenotype did not provide information on specific types of diabetes, another phenotype *type 2 diabetes (self-reported)* also showed similar association patterns. The involvement of body iron overload in diabetes has been frequently reported [30], with a recent brain imaging study showing increased χ in caudate, putamen and pallidum in type 2 diabetes patients compared with healthy controls, which agrees with our results [31]. This suggests potential associations between iron accumulation in subcortical structures and diabetes.

Mental health

In the mental health category, 4 phenotypes were significantly associated with subcortical QSM IDPs. For example, QSM in the right pallidum, and left/right substantia nigra IDPs were associated with *risk taking* where the strongest correlation was with QSM in the right substantia nigra ($r = 0.037, P = 1.29 \times 10^{-11}$). The voxel-wise association map with *risk taking* (**Fig. 4e**) revealed spatially contiguous associations in substantia nigra and sub-regions of the

pallidum. Although the right pallidum IDP was associated with *seen doctor (general practitioner, GP) for nerves, anxiety, tension or depression* ($r = 0.028, P = 1.26 \times 10^{-7}$), the voxel-wise association map (**Fig. 4f**) revealed spatially contiguous associations predominantly in the substantia nigra region, whereas correlations in the pallidum region were not as strong. We also found that QSM in right the caudate, left/right putamen and left/right substantia nigra were associated with *ever taken cannabis*, where the strongest correlation was with left putamen ($r = 0.049, P = 2.96 \times 10^{-14}$). Voxel-wise association map with *ever taken cannabis* (**Fig. 4g**) revealed spatially contiguous associations in putamen, substantia nigra, sub-regions of thalamus and caudate, but also in the red nucleus and cerebellar regions for which we have not generated IDPs.

Alcohol consumption

Phenotypes in the alcohol consumption category demonstrate stronger correlations with QSM IDPs compared with T2* in the putamen, caudate and thalamus (**Fig. 3a, b**). These results agree with a previous study finding higher χ in the putamen and caudate in subjects with alcohol use disorder [32], which likely reflects abnormal iron accumulation in these structures. Furthermore, phenotypes relating to the quantity of alcohol consumption, such as *frequency of consuming six or more units of alcohol*, showed significant negative correlations with χ in thalamus, but no significant correlation with T2* ($r = -0.043, P = 1.15 \times 10^{-10}$ and $r = -0.0063, P = 0.3427$ respectively, right thalamus). The thalamus has been reported as a key region in alcohol use disorder due to its involvement in two brain networks (the frontocerebellar circuit and Papez circuit) that are particularly affected by alcohol consumption [33,34]. Although no previous studies have linked χ in thalamus with alcohol use disorder, many neuroimaging studies have reported thalamic volume changes and decreased connectivity in thalamus in alcohol use disorder patients [33,34]. One possible unifying explanation for this literature and our results (negative correlations between thalamic χ and heavy alcohol consumption) would be microstructure differences in thalamic white matter. Voxel-wise association map with *frequency of consuming six or more units of alcohol* (**Fig. 4h**) revealed clusters in the putamen, caudate and sub-regions of thalamus, but also in sub-regions of the substantia nigra. These nigral correlations additionally agree with previous reports of increased χ in the substantia nigra of alcohol use disorder patients [32].

Phenotypic associations with QSM white matter hyperintensity IDP

Association analyses between QSM in white matter hyperintensities and phenotypes are shown in **Fig. 2c**. In total, 71 phenotypes were significantly associated with QSM WMH IDP (Details are provided in **Supplementary Table 1**). For example, without regressing out the WMH volume IDP, the QSM WMH IDP showed significant associations with 65 phenotypes. The strongest correlation was found between the QSM WMH IDP and *multiple sclerosis (self-reported)* phenotype in the health outcomes category ($r = -0.068$ and $P = 2.13 \times 10^{-37}$). Regressing out WMH volume generally reduced association strength, however, correlation between QSM WMH IDP and *multiple sclerosis (self-reported)* remained significant ($r = -0.030$ and $P = 3.21 \times 10^{-8}$, after regressing out WMH volume). Correlations with blood pressure related phenotypes such as *diastolic blood pressure* showed an increase in association strength after regressing out WMH volume (from non-significant, $r = -0.0096$, $P = 0.0831$ to significant, $r = 0.037$, $P = 5.27 \times 10^{-11}$). White matter hyperintensity has been associated with multiple factors including ageing, hypertension, cerebrovascular diseases and multiple sclerosis [35]. Our results demonstrate that the χ difference between WMH lesions and normal-appearing white matter might provide insights into the underlying mechanisms of

different causes of WMH (for example, multiple sclerosis versus hypertension), particularly given that associations with *diastolic blood pressure* and *multiple sclerosis (self-reported)* showed opposite signs.

Associations between IDPs and genetic variants

Heritability estimates for subcortical QSM and T2* IDPs

Following the approach described in refs. [36,37], we examined the heritability of each subcortical IDP using linkage score regression [38]. This method estimates the fraction of phenotypic variance that is explained by additive effects from genetic variants (this is h^2, or narrow sense heritability [39]). This score ranges from 0 to 1 with 0 meaning that the phenotypes of two samples with the same genotype are independent and 1 meaning that the phenotypes of two samples with the same genotype are identical.

The heritability estimates for all subcortical QSM and T2* IDPs are shown in **Fig. 5a**. The estimated h^2 value for each of the subcortical IDPs was more than one standard error greater than 0, indicating that all subcortical IDPs had high levels of heritability. QSM IDPs generally showed higher heritability than T2* IDPs. Putamen showed the highest heritability among 8 subcortical regions (ranging from 0.303 to 0.342), while amygdala and accumbens showed two of the lowest heritability estimates (ranging from 0.0357 to 0.124). In previous work [37], heritabilities of brain IDPs in UK Biobank were found to lie in the range of [0.000, 0.405]. A heritability of 0.342 for putamen places it in the upper 98-th quantile among UK Biobank brain IDPs (and an h^2 of 0.342 corresponds to roughly half the narrow sense heritability of human height [39]).

Genome-wide associations studies of IDPs

We carried out a genome-wide association study (GWAS) for each of the QSM and T2* IDPs (16 subcortical IDPs and 1 WMH IDP with/without regressing out WMH volume), following a previously-described approach [36,37]. We used the second UK Biobank release of imputed genetic data, comprising over 90 million genetic variants. Subjects with available χ maps were divided into a discovery cohort (19,720 subjects) and a replication cohort (9,859 subjects). The standard single-phenotype GWAS threshold ($-\log_{10}P = 7.5$) and also a more stringent threshold after additional Bonferroni correction to account for the number of GWASs (16 + 2) carried out (resulting in a 'Bonferroni' threshold of $-\log_{10}P = 8.76$) were used. For each GWAS, the genetic variant with the highest association with an IDP in each region of high linkage disequilibrium (LD) was reported as a peak association (see Methods). Manhattan plots for each of the GWASs were produced, plotting the $-\log_{10}P$ value for each genetic variant. Two example Manhattan plots are shown in **Fig 5b, c** (More plots are provided in Supplementary Material, Section 5). A summary of peak associations identified in all GWASs is provided in **Table 1**. The full list of peak associations is provided in **Supplementary Table 2, 3**.

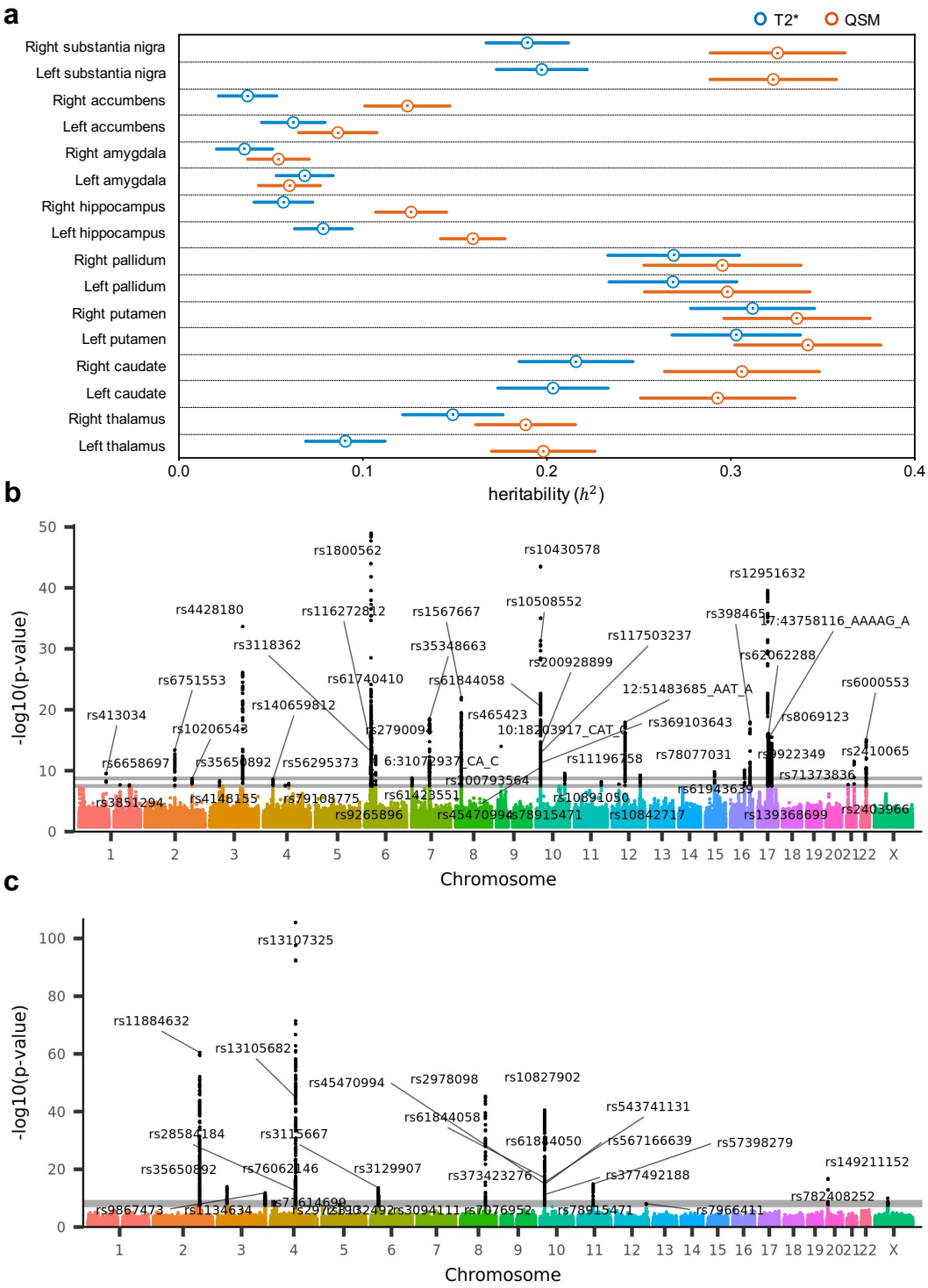

Figure 5 (a) Heritability estimates (h^2) for subcortical QSM and T2* IDPs grouped according to regions. Circle indicates heritability estimate and error bar indicates standard error. **(b)** Example Manhattan plot relates to the GWAS for the QSM right putamen IDP. **(c)** Example Manhattan plot relates to the GWAS for the QSM right pallidum IDP. The lower grey line indicates the $-\log_{10}P$ threshold of 7.5 and the upper line the Bonferroni threshold of 8.76.

Table 1 Summary of lead associations with all QSM and T2* IDPs

ROI	Discovery (N=19,720)				Replication (N=9,859)			
	N_{SNPs} ($-\log_{10}P_{dis} \geq 7.5$)		N_{SNPs} ($-\log_{10}P_{dis} \geq 8.76$)		N_{SNPs} ($-\log_{10}P_{dis} \geq 7.5$ & $P_{rep} < 0.05$)		N_{SNPs} ($-\log_{10}P_{dis} \geq 8.76$ & $P_{rep} < 0.05$)	
	QSM	T2*	QSM	T2*	QSM	T2*	QSM	T2*
Thalamus (L)	9	4	5	3	8	4	5	3
Thalamus (R)	6	4	6	3	6	3	6	2
Caudate (L)	36	26	27	22	30	22	24	21
Caudate (R)	34	28	27	22	30	26	27	22
Putamen (L)	41	37	36	31	39	34	36	30
Putamen (R)	49	41	36	36	43	38	34	34
Pallidum (L)	35	25	31	20	33	22	30	18
Pallidum (R)	29	30	24	23	25	27	24	22
Hippocampus (L)	4	0	3	0	3	0	3	0
Hippocampus (R)	4	0	3	0	4	0	3	0
Amygdala (L)	2	0	0	0	2	0	0	0
Amygdala (R)	1	0	1	0	1	0	1	0
Accumbens (L)	1	0	1	0	1	0	1	0
Accumbens (R)	2	1	1	0	2	0	1	0
substantia nigra (L)	14	12	11	10	14	9	11	9
substantia nigra (R)	17	10	15	9	16	10	14	9
WMH	4	4	3	2	4	3	3	2
WMH (WMHV out)	4	3	2	2	4	2	2	1
Subtotal	292	225	232	183	265	200	225	173
Total	517		415		465		398	

The $-\log_{10}P_{dis}$ and $P_{rep} < 0.05$ values provided are for the main discovery and replication cohorts, respectively. 'WMHV out' represents regressing out the WMH volume IDP.

We then fed the GWAS results of all IDPs into the Peaks software package [37] to automatically generate clusters of peak associations between genetic variants and IDPs. A cluster is defined using the discovery cohort as a set of IDP-variant pairs for which all genetic variants are within a 0.25-cM distance of the top variant (from an IDP-variant pair with highest $-\log_{10}P$ value) in the cluster. We classify a cluster as replicating if at least one of its IDP-variant pairs had nominal significance ($P < 0.05$) in the replication cohort. We then used FUMA [40] to map the top genetic variant of each cluster to related genes and expression quantitative trait loci (eQTL).

We identified 88 distinct clusters of peak associations, with 80 clusters replicating. Among the replicated clusters, 55 were observed in both QSM and T2* IDPs, 22 were unique to QSM IDPs, and only 3 were unique to T2* IDPs. All clusters common to both QSM and T2* IDPs replicated. A summary of 18 example clusters is provided in **Table 2**. The full list of the 88 clusters is provided in **Supplementary Table 4**.

Table 2 Information for the 18 example genetic clusters

Related function	Cluster #	IDP	N_{pair}	RSID	gene	a1	a2	$-\log_{10}P_{dis}$
Iron homeostasis	6	QSM_L_PAL	15	rs11884632	*SLC40A1*	G	C	71.271
	10	T2star_L_PUT	18	rs4428180	*TFP1:TF*	A	G	42.458
	12	QSM_L_SN	7	rs9867473	*TFRC*	A	C	14.562
	27	QSM_R_PUT	21	rs1800562	*HFE*	G	A	48.973
	65	QSM_L_THA	1	rs1131488	*HMBS*	G	T	7.8271
Zinc transport	15	QSM_R_PAL	18	rs13107325	*SLC39A8*	C	T	105.51
	47	QSM_L_CAU	24	rs4348791	*SLC39A12*	T	C	100.55
Calcium homeostasis	49	QSM_R_CAU	10	rs11012783	*CACNB2*	A	G	75.579
	60	T2star_R_CAU	3	rs11013321	*CACNB2*	C	G	9.0318
	67	T2star_R_PUT	3	rs73192811	*TPCN1*	G	T	10.406
	69	QSM_R_PUT	1	rs10842717	*ITPR2*	G	A	7.7763
	16	QSM_L_PAL	12	rs13105682	*BANK1*	T	G	46.911
	18	QSM_L_PAL	7	rs76062146	*BANK1*	G	A	14.353
	20	QSM_L_PAL	2	rs71614699	*BANK1*	A	G	10.914
Myelin and Glia	11	QSM_L_PAL	3	rs34457487	*MOBP*	G	A	15.932
	73	QSM_L_PUT	3	rs7203922	*PLLP*	C	T	10.575
	79	QSM_L_THA	4	rs1126642	*GFAP*	C	T	11.181
Extracellular matrix	25	QSM_WMH	2	rs10052710	*VCAN*	T	G	18.745

Columns IDP and RSID represent the top IDP/variant pair in each group. Column N_{pair} indicates the number of phenotype/variant pairs included in each genetic cluster. Columns a1 and a2 indicate the reference allele and alternate allele of the variant. The $-\log_{10}P_{dis}$ values provided are for the main discovery cohort.

The majority of the 88 genetic clusters could be associated with genes, including 11 clusters with variants in exons (8 missense, 3 synonymous). Many of these clusters are associated with genes involved in functions expected to affect tissue χ, such as myelination, iron and calcium homeostasis. However, many clusters were associated with genes that were not expected to have a direct effect on tissue χ, such as genes encoding transcription factors, extracellular matrix proteins, and proteins acting on intracellular trafficking. Below, we describe a few example genetic clusters in more detail.

Iron transport and homeostasis

Multiple clusters with strong associations were related to genes implicated in iron transport and homeostasis. For example, **cluster 6** comprises eight genetic variants in LD, in close proximity to or in introns of the ferroportin gene (*SLC40A1*). These variants associated with QSM and T2* IDPs in the pallidum, substantia nigra and putamen and T2* IDPs in the accumbens and caudate. Ferroportin acts on the export of iron ions, and mutations in the ferroportin gene lead to hemochromatosis [41].

We also observed associations with variants related to the transferrin gene (*TF*, **cluster 10**, top variant rs4428180), to the transferrin receptor gene (*TFRC*, **cluster 12**), and to the homeostatic iron regulator gene (*HFE*, **cluster 27**, top variant rs1800562). Transferrin (TF) is a circulating protein that delivers iron to all proliferating cells in the body via the transferrin receptor (TFRC). The homeostatic iron regulator protein (HFE) regulates the interaction of the transferrin receptor with transferrin, thus regulating iron absorption. Mutations in the *HFE* gene lead to hereditary hemochromatosis (MIM 235200), while mutations in *TF* lead to hereditary atransferrinemia (MIM 209300) [41]. Variants observed in our study have been previously associated with multiple traits including transferrin levels [42], iron biomarkers [43], and increased risk of developing Alzheimer's disease [44]. The voxel-wise association map with variant rs11884632 (*SLC40A1*) (**Fig. 6a**) revealed spatially contiguous associations in the pallidum, sub-regions of substantia nigra and thalamus, but also in the red nucleus and cerebellar nuclei regions for which we haven't generated IDPs. Voxel-wise association maps with variant rs1800562 (*HFE*) (**Fig. 6b**) revealed spatially contiguous associations in the putamen, substantia nigra, sub-regions of caudate and thalamus, as well as in the red nucleus and cerebellar regions. Interestingly, associations with variants related *SLC40A1* (positive) and *HFE* (negative) had opposite signs in corresponding regions, which is in line with their biological functions (that is, *SLC40A1* regulates export of iron while *HFE* regulates iron absorption).

In addition, we observed variants in genes related to the synthesis of heme groups. For example, QSM in left thalamus was associated with an exonic synonymous variable with a high deleteriousness score (CADD: 17.8) in the *HMBS* gene (**cluster 65**, top variant rs1131488). *HMBS* encodes an enzyme from the heme biosynthetic pathway, and mutations are associated with acute intermittent porphyria [45] and leukoencephalopathy, for which anomalies in the thalamus and cerebral white matter can be identified with MRI [46]. This gene was not found to be associated with any T2* IDPs. The voxel-wise association map with variant rs1131488 (*HMBS*) (**Fig. 6c**) revealed spatially contiguous associations in sub-regions of thalamus and in white matter regions.

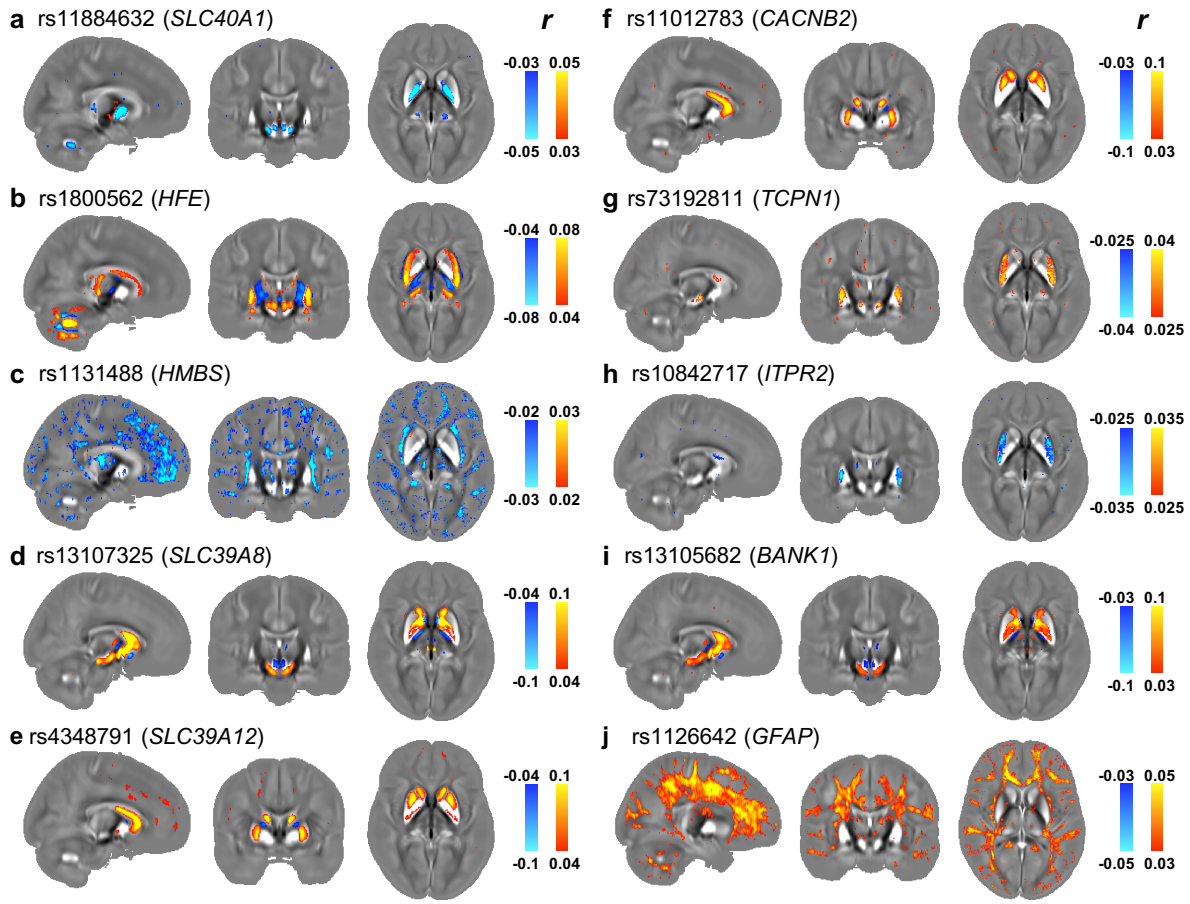

Figure 6 Voxel-wise association maps of 9 example top genetic variants with susceptibility maps aligned in MNI space. In associations with QSM IDPs, **(a)** rs11884632 (*SLC40A1*) was associated with QSM IDPs in caudate, putamen, pallidum and substantia nigra; **(b)** rs1800562 (*HFE*) was associated with QSM IDPs in thalamus, caudate, putamen, hippocampus and substantia nigra; **(c)** rs1131488 (*HMBS*) was only associated with QSM left thalamus IDP; **(d)** rs13107325 (*SLC39A8*) was associated with QSM IDPs in caudate, putamen, pallidum, substantia nigra and WMH IDP (both with and without regressing out the WMH volume IDP); **(e)** rs4348791 (*SLC39A12*) was associated with QSM IDPs in caudate, putamen, pallidum, substantia nigra and WMH IDP (with regressing out the WMH volume IDP); **(f)** rs11012783 (*CACNB2*) was associated with QSM IDPs in caudate, putamen and pallidum; **(g)** rs73192811 (*TPCN1*) was associated with QSM IDPs in putamen; **(h)** rs10842717 (*ITPR2*) was only associated with QSM right putamen IDP; **(i)** rs13105682 (*BANK1*) was associated with QSM IDPs in caudate, pallidum and substantia nigra; ; **(j)** rs1126642 (*GFAP*) was associated with QSM IDPs in thalamus and hippocampus;

Zinc transporters

We observed associations with variants in genes related to the transport of other minerals in addition to iron. Three clusters were associated with genes from the SLC39 family of solute-carriers, which is characterized as zinc transporters but can also act on the transport of other metal ions, including iron. For example, **cluster 15** comprises four genetic variants associated with QSM and T2* IDPs in multiple subcortical structures and white matter hyperintensity. The top variant (rs13107325) is a missense variant of *SLC39A8* (also known as *ZIP8*). *SLC39A8* encodes a transmembrane protein that acts as a transporter of several divalent cations, including zinc and iron. Mutations in this gene can lead to congenital disorder of glycosylation, a multisystem developmental disorder with intellectual disability (MIM 616721) [47,48]. This genetic variant has been linked to a large number of traits, including those linked to blood

pressure [49], diabetes [50], Parkinson's disease and schizophrenia [51,52], alcohol consumption [53], haemoglobin and haematocrit [54] and brain morphology [36,55,56]. Voxel-wise association map with rs13107325 (*SLC39A8*) (**Fig. 6d**) revealed spatially contiguous associations in the caudate, substantia nigra, pallidum and sub-regions of putamen.

Cluster 47 comprises eleven genetic variants associated with QSM and T2* in the caudate, putamen, pallidum, substantia nigra and QSM white matter hyperintensity IDP (after regressing out WMH volume). This cluster includes genetic variants that are, in LD with, and eQTL of the *SLC39A12* gene (top variant rs4348791). *SLC39A12* encodes a zinc/iron transmembrane transporter that is highly expressed in the brain. Low expression of *SLC39A12* leads to reduced intracellular zinc and reduced polymerization of N-tubulin, with impaired neural development as a consequence [57]. The voxel-wise association map with rs13107325 (*SLC39A12*) (**Fig. 6e**) revealed spatially contiguous associations in the caudate, putamen and pallidum.

Interestingly, variants in these two genes from the SLC39 family both showed significant association with QSM across the whole caudate regions, however, variants in *SLC39A8* showed stronger association in pallidum while variants in *SLC39A12* showed stronger association in putamen.

Calcium homeostasis

Four clusters were related to genes encoding three calcium channel proteins. **Cluster 49** comprises two genetic variants associated with QSM and T2* in the caudate, pallidum and putamen, and **cluster 60** comprises of two genetic variants associated with QSM and T2* in the caudate. These two clusters contained variants that are, in LD with, and eQTL of the *CACNB2* gene. *CACNB2* encodes a beta subunit of voltage gated calcium channels that control the influx of calcium from the extracellular space. In these channels, the beta subunit promotes the trafficking of channel proteins to the plasma membrane and regulates its function [58]. Variants in this gene have also been associated with autism, bipolar disorder, depression and schizophrenia [59–61]. Voxel-wise association map with rs11012783 (*CACNB2*) (**Fig. 6f**) revealed spatially contiguous associations in the caudate and sub-regions of putamen.

Cluster 67 comprises of two intronic variants in the *TPCN1* gene that were associated with QSM and T2* in the putamen, and **cluster 69** comprises of one genetic variant in an intron of *ITPR2* that was associated with QSM in the right putamen. Both *TCPN1* and *ITP2* encode calcium channels that control the release of calcium from intracellular spaces. *TCPN1* encodes a voltage gated Ca2+ and Na2+ channel involved in signalling pathways, regulation of autophagy, and in the modulation of endolysosomal iron release [62,63], whereas *ITPR2* encodes an endoplasmic reticulum calcium channel that mediate raises in intracellular calcium content and is involved in many processes including neuronal signalling [64]. Interestingly, we observed similar spatial pattern (spatially contiguous associations in the putamen) with opposite signs on voxel-wise association maps with rs73192811 (*TCPN1*, positive) (**Fig. 6g**) and rs10842717 (*ITPR2*, negative) (**Fig. 6h**).

In addition, three clusters associated with QSM and T2* in the pallidum, caudate and substantia nigra are related to *BANK1* including **clusters 16**, **clusters 18** and **clusters 20** (top variants: rs13105682, rs76062146 and rs71614699)**.** *BANK1* encodes a protein known to regulate calcium mobilization from intracellular stores in B-cells and that is primarily related to the immune system, but is also expressed in the brain (mostly in microglia). Variants in *BANK1*

have been related to working memory task-related brain activation [65]. Voxel-wise association map with rs13105682 (*BANK1*) (**Fig. 6i**) revealed spatially contiguous associations in the caudate, substantia nigra and sub-regions of pallidum.

Glia and myelin

We observed associations with genetic variants in two genes that encode structural constituents of myelin sheaths. **Cluster 73** (top variant rs7203922) comprises of two genetic variants associated with QSM and T2* in the putamen. These genetic variates are in, or in close proximity to, the *PLLP* gene, which encodes the myelin protein plasmolipin. **Cluster 11** (top variant (rs34457487) comprises of two genetic variants associated with QSM in the pallidum and putamen. Both variants are located in an intron of *MOBP*, which encodes the myelin-associated oligodendrocyte basic protein.

In addition, **cluster 79** (top variant rs1126642) comprises of three genetic variants associated with QSM in the thalamus and hippocampus and T2* white matter hyperintensity IDP (without regressing out the hyperintensities volume). The top variant (rs1126642) is a missense variant of *GFAP*, which encodes an intermediate filament protein highly specific for cells of astroglial lineage. Mutations in *GFAP* lead to Alexander disease, a genetic disorder characterized by fibrinoid degeneration of astrocytes, demyelination and white matter anomalies [66]. Variants in this gene have been associated with white matter microstructure phenotypes and Alzheimer's disease [56,67,68]. While astrocytes are present in both grey and white matter, *GFAP* expression is higher in white matter astrocytes than in grey matter astrocytes [69]. Voxel-wise association map with rs1126642 (*GFAP*) (**Fig. 6j**) revealed spatially contiguous associations in the thalamus and widespread white matter regions.

Extracellular matrix

We identified many genetic associations that do not have an obviously direct link to magnetic susceptibility contrast. For example, **cluster 25** comprises one genetic variant (rs10052710) located in an intron of *VCAN* and associated with QSM white matter hyperintensity IDP (both with/without regressing out the hyperintensity volume). *VCAN* encodes versican, a large chondroitin sulphate proteoglycan that is a major component of the extracellular matrix in multiple tissues including the brain, and that is highly expressed in the brain during development [70]. In addition to its structural role, versican can also interact with inflammation and the immune response [71], and its expression is altered in multiple sclerosis lesions [72,73]. This and other variants in *VCAN* have been previously associated with multiple brain phenotypes, in particular to white matter microstructure metrics derived from diffusion MRI [36,56,74].

DISCUSSION

Quantitative susceptibility mapping in population imaging

QSM has been shown to be quantitatively related to specific tissue constituents. For example, χ has been demonstrated to have a strong, positive linear relationship with iron concentration (measured using mass spectrometry) in post-mortem brain tissues [26]. χ values in white matter and calcified lesions have also been validated using myelin staining intensity [75] and CT attenuation values [76]. In our reproducibility analysis using the two-timepoint data from 1,447 subjects (**Supplementary Fig. S13**), we found high cross-scan correlations ($r > 0.8$) for χ in 4 subcortical regions (caudate, putamen, pallidum and substantia nigra) and they are all higher

than corresponding T2* IDPs ($0.6 < r < 0.8$). In heritability analysis, these 4 regions also showed the highest heritability among all QSM and T2* IDPs (**Fig. 5a**), which are at a similar level to other IDPs found to be most heritable across all available brain IDPs in UK Biobank [37]. Notably, these 4 regions showed the highest susceptibilities among all ROIs and have been reported to have the highest iron concentrations in the brain [77,78]. These observations suggest that in structures where iron is the dominant χ source, QSM is able to provide an accurate, reproduceable quantification of tissue iron levels.

QSM has been used in studies of neurological disorders including neurodegenerative diseases (for example, Alzheimer's Disease, Parkinson's disease and amyotrophic lateral sclerosis) and neuroinflammatory diseases (for example, multiple sclerosis). However, unlike structural, diffusion, and fMRI data that have been collected in existing large-scale imaging studies consisting of thousands of subjects (for example, the Enhancing Neuro Imaging Genetics through Meta-Analysis (ENIGMA) consortium [79]), QSM has only been used in smaller-scale studies with clinically-defined cohorts. This new UK Biobank QSM resource is by approximately 2 orders of magnitude the largest QSM dataset that has ever been collected [9], which is particularly powerful as a result of the combination of the number of subjects and the breadth of linked data including genetics, extensive phenotyping and health outcomes. At the time of scanning, most UK Biobank subjects are largely healthy, with the cohort age range chosen such that health outcomes will begin to accumulate in the coming decades. Hence, this cohort is particularly appropriate for the study of age-associated pathology. For example, in the imaged cohort, thousands of participants are expected to develop Alzheimer's and Parkinson's diseases by 2030 [80].

Although QSM has been much less explored in mental health conditions compared to neurodegeneration, in this study, we have identified associations between several mental health phenotypes. Our results suggest that QSM may serve as a potential quantitative imaging tool in the study of mental health conditions.

Producing accurate and reproduceable χ maps for a dataset at this scale requires a robust, fully automated QSM processing pipeline [14]. Until now, no such pipeline existed for UK Biobank swMRI data. Thus, we investigated a number of existing phase-processing algorithms to identify an optimal QSM pipeline for the UK Biobank swMRI data (Supplementary material Section 1.1). We also introduced a new brain masking procedure to automatically detect and exclude voxels with extremely large phase variances, a major source of imaging artefacts most apparent in the vicinity of sinus cavities (Details are provided in Supplementary Material Section 1.1).

The variability of χ estimates we observed across different combinations of processing algorithms clearly demonstrated that although QSM is a quantitative technique, it is crucial to use matched processing pipelines for harmonisation of QSM results across sites or vendors. Thus, the dissemination of our pipeline is important to the translational impact of the UK Biobank QSM resource. For example, in order to relate a new subject to a classifier trained using UK Biobank data [81] or to a nomogram derived from UK Biobank [82], it will be important to use the same QSM processing pipeline. To date, two ongoing COVID-19 brain imaging studies have already adopted our QSM pipeline (C-MORE/PHOSP and COVID-CNS) [83] to process their brain swMRI data.

Phenotypic and genome-wise associations with QSM data

Above, we presented a few example phenotypic associations in detail, which correspond to approximately 10% of all phenotypes associated with QSM IDPs. There is thus a rich set of associations that remains to be explored. Some of these phenotypes have previously-established links to χ measures in the brain (for example, smoking), but many phenotypes may not have an easily interpretable relationship with χ measures (particularly in lifestyle categories). For example, multiple factors could be involved in the associations between *use of sun/uv protection* and QSM IDPs in caudate and putamen. Furthermore, given that grey and white matter have sharp boundaries on χ maps due to the opposite signs of χ (particularly around subcortical structures), QSM data are particularly sensitive to atrophy. Hence, some phenotypic associations with QSM IDPs may be driven by edge effects rather than χ changes within the ROI. For example, QSM substantia nigra IDPs were found to have an apparent association with *total BMD (bone mineral density)*. However, the voxel-wise map with *total BMD* revealed spatially contiguous associations along the boundaries between subcortical structure and surrounding white matter bundles which is consistent with an edge effect that may simply reflect atrophy (**Supplementary Fig. S25a,b**). Interestingly, the voxel-wise association map with *body mass index (BMI)* revealed stripe-shaped spatially contiguous associations (interleaved positive/negative signs of correlation) in the primary motor and somatosensory areas (**Supplementary Fig. S25c,d**).

We described example genetic associations (18 of the 88 genetic clusters) in detail, all of which have a clear link to tissue χ. However, we also observed many associations with genetic variants related to other biological functions that are not known to be directly related to tissue χ, including immune response, regulation of gene expression, and proteins related to cell function such as vesicle trafficking (Supplementary Material, Section 6). This rich set of genetic associations will hopefully promote additional studies to further explore the genetic architecture of magnetic susceptibility in the brain.

Iron and calcium in quantitative swMRI

The strongest phenotypic associations with QSM and T2* IDPs was found to be body iron markers (haemoglobin), and in GWAS, QSM and T2* IDPs were strongly associated with many genetic variants in genes involved in iron homeostasis.

Iron, an essential transition metal, is involved in many fundamental biological processes in the brain including neurotransmitter production, myelin synthesis and many metabolic processes [84,85]. Iron homoeostasis is essential to maintain normal physiological brain function, whereas elevated iron levels can cause oxidative stress and cellular damage [84,85]. Progressive accumulation of iron occurs in several brain regions during healthy aging [84,85]. However, abnormal iron accumulation is associated with many neurodegenerative diseases that are prevalent in aging population, including Alzheimer's disease, Parkinson's disease, and multiple sclerosis [84,85]. Despite considerable investigation, it is still not clear whether abnormal iron accumulation in the brain is an initial event that causes neuronal death or is a consequence of the disease process [84,85].

In this study, many strong associations with variants in genes encoding calcium channels were identified. While it has been demonstrated that calcifications lead to alterations in tissue χ, little is known about the impact of other calcium forms on tissue χ. Calcium is essential for many aspects of cell functioning, such as neurotransmitter and hormone release, muscle excitation-contraction coupling, cell division, differentiation, migration, and cell death [58]. Perturbations

in calcium homeostasis (including dysregulation of calcium channel activities) have been reported in many neurodegenerative disorders [86,87].

Hence, assessing the impact of altered iron and calcium homeostasis using quantitative swMRI in UK Biobank has great potential to shed light on the causality between abnormal iron accumulation (and potential dysregulation of calcium signalling) at the pre-symptomatic stage and onset of neurodegeneration and other age-related diseases. These measures could provide predictive markers for preventative stratification, treatment monitoring and imaging-based screening.

T2* and QSM in UK Biobank

Due to the limited scan time, UK Biobank swMRI data has only two echoes, which is the minimum required to perform T2* mapping. Under these circumstances there is no distinction between signal and noise components when fitting, resulting in T2* estimates that are very sensitive to the contribution of noise. However, QSM, in theory, can be calculated from just a single echo (because this model has a single parameter χ).

In addition, estimation of T2* is well-known to be confounded by the presence of macroscopic field gradients that are induced by proximal air/tissue interfaces or poor shim quality [24], particularly when acquiring thick slices as in the UK Biobank data [24]. If not properly deconfounded, this could lead to spurious correlations that are driven by subject-wise variations in field homogeneity. In this study, we introduced a set of confounds for T2* IDPs to account for macroscopic field gradients (details are provided in the Supplementary Material, Section 2). However, QSM is not confounded by this effect, as evidenced by the very low correlation with macroscopic field gradients in our QSM data (**Supplementary Fig. S18**).

Importantly, our results suggest that QSM and T2* contribute unique information, as reflected in the existence of different patterns of associations for these two IDP categories. For example, because diamagnetic and paramagnetic constituents are manifested differently in QSM and T2* data, the combination of QSM and T2* will enable us to decompose the potential co-occurring changes of tissue iron and myelin content in neurodegeneration. Thus, our QSM data will be a valuable addition to UK Biobank brain imaging resource that provides complementary information to all existing brain imaging measures in UK Biobank.

Methods

MRI Data acquisition and participant information

We used data from 35,885 participants in UK Biobank early-2020 release who had susceptibility-weighted MRI (swMRI) data collected. Participants were 53.11% female and aged 45-82yo (64.04±7.5yo) at time of imaging. Of these participants, 1,447 were recruited for a repeat scan approximately 2 years (2.25±0.12y) after the first imaging session. A detailed overview of the neuroimaging acquisition protocols used in UK Biobank brain imaging are described in Miller et al. [11].

Susceptibility-weighted MRI scans were acquired on 3T Siemens Skyra MRI scanners (software platform VD13) with 32-channel head receive coils. swMRI data were acquired using a three-dimensional (3D) dual-echo gradient echo (GRE) sequence with the following

parameters: voxel size = 0.8 x 0.8 x 3 mm^3, matrix size = 256 x 288 x 48 (whole-brain coverage), echo times (TE1/TE2) = 9.4/20 ms, repetition time (TR) = 27 ms and in-plane acceleration = 2, total scan time = 2:34 min. Magnitude and phase data from each receive channel were saved for off-line coil combination, described below [12].

The UK Biobank brain imaging protocol includes T1- and T2-weighted structural acquisitions that are used in our processing pipeline [12]. Specifically, the T1-weighted structural scan is used to align subjects into a standard-space atlas for definition of regions-of-interest and other masks, and T2 FLAIR data is used to generate ventricle masks used in QSM referencing. Specifically, brain region masks and image registration references were derived from T1-weighted structural scans acquired using a 3D MPRAGE protocol (voxel size = 1 x 1 x 1 mm^3, matrix size = 208 x 256 x 256, inversion time (TI)/TR = 880/2000 ms, in-plane acceleration = 2, total scan time = 4:54 min) [12]. Ventricle and white matter hyperintensity masks were derived from T2-weighted fluid attenuated inversion recovery (FLAIR) scans (3D SPACE, voxel size = 1.05 × 1 × 1 mm^3, matrix size = 192 x 256 x 56, TI/TR = 1800/5000 ms, in-plane acceleration = 2, total scan time = 5:52 min) [12]. Both T1 and T2 weighted structural data were processed using the UK Biobank image processing pipeline [12].

The quality control (QC) pipeline developed for UK Biobank brain imaging [12] was applied to all subjects included in this study. Several QC measures related to T1-weighted, T2 FLAIR and swMRI data were used here. For example, subjects were excluded if registration from T1 space to standard space failed or had unusable T2 FLAIR data, for example due to excessive head motion, atypical structure and/or anatomical abnormalities. Full details of the quality control pipeline are described in Alfaro-Almagro et al. [12]. Finally, 35,273 participants were selected in this study whose data were deemed suitable for quantitative susceptibility mapping analysis based on QC measures.

Quantitative susceptibility mapping processing pipeline

Quantitative susceptibility mapping (QSM) consists of several steps including combination of phase data from individual channels, unwrapping of channel-combined phase data, removal of macroscopic ('background') field inhomogeneity, and estimation of voxel-wise χ through dipole inversion (**Fig. 1a**). For each step, many different algorithms have been proposed [14,88,89]. To ensure the robustness of our QSM pipeline and select the optimal pipeline for the UK Biobank protocol, we carried out extensive evaluations of established algorithms for each step of the QSM pipeline on a subset of approximately 1,500 subjects [17–21,90–94]. These evaluations used both quantitative and qualitative metrics, including the presence of streaking artifacts, the observation of large-scale field inhomogeneities on χ maps and cross-subject consistency of both χ maps (in standard space) and χ values in regions of interest (such as subcortical structures). Details of our QSM processing pipeline evaluations are described in the Supplementary Material (Section 1.1).

QSM provides a measure of relative, rather than absolute χ [89]. The presence of an unknown offset in the estimated map for any individual is problematic for comparison of χ values across subjects. To address this, χ values are commonly reported as relative offset with respect to an internal reference region [89,95]. In this study, we compared the use of three widely-used reference regions: mean χ across (i) the whole brain, (ii) cerebrospinal fluid (CSF) and (iii) a white matter region (forceps minor). Evaluations were performed using subjects who had undergone scanning at two time points (1,447 subjects in total). Specifically, we calculated cross-scan correlations for each of the subcortical QSM IDPs (referenced to these three different regions)

as well as subcortical T2* IDPs, with the assumption that negligible changes in χ/T2* occurred during the two timepoints. CSF-referenced QSM IDPs showed the highest consistency (correlation r) across two time points (**Supplementary Fig. S13a**) and CSF in the lateral ventricles was therefore chosen as the reference region. Details of the evaluation of three reference regions are described in the Supplementary Material (Section 1.2). The final QSM processing pipeline for UK Biobank swMRI data is as follows:

In order to generate a map of the image phase, we first need to combine (average) phase images from individual coil channels. The challenge is that each coil channel has a different unknown phase offset that will cause phase cancellation if it is not first removed. Our pipeline combines phase images across channels using the MCPC-3D-S approach [17]. Specifically, a channel-combined phase image was first estimated using the phase difference method (via complex division of two echoes' phase data, yielding an equivalent $TE = TE_1 - TE_2$), masked using the brain mask provided by the UK Biobank image processing pipeline [12], and then unwrapped using PRELUDE [96]. This unwrapped phase image was scaled to correspond to $TE = TE_1$ and then subtracted from each channel's first echo phase image respectively to estimate the phase offset for each channel. The estimated phase offsets were subsequently smoothed in the complex domain and subtracted from the phase images (both echoes) of all channels prior to combination. Using this approach, a channel-combined phase image free from any phase cancellation artifacts was generated for each echo.

The brain masks used in this study were based on those used in the standard UK Biobank image processing pipeline [12]. These masks were refined for QSM to detect and remove voxels in the vicinity of sinus cavities. These regions have extremely strong field variations due to the air/tissue interface that induce artifacts in the χ maps. For each echo, we generated a phase reliability map as follows. Channel-combined phase images were converted to complex data (assuming unit magnitude values) and convolved with a 3D spherical kernel (2mm in radius with probabilistic values for voxel locations inside the kernel) for voxels within the brain mask (only voxels within the intersection of the kernel and brain mask were included for convolution). Our phase reliability map was then derived by calculating the magnitude of the convolved complex data: regions of strong phase variation were indicated by low magnitude values due to phase cancellation within the convolution kernel, while regions with relatively homogeneous phase had magnitude values close to one. Here, the refined mask excluded voxels with phase reliability values lower than 0.6 for the first echo, and 0.5 for the second echo. An additional step was then applied to the refined brain mask to fill any isolated holes (in 3D) in the middle of the bran that were not connected to the sinus cavities using the MATLAB function "imfill".

The channel-combined phase images were unwrapped using a Laplacian-based algorithm provided by the STI Suite toolbox [18]. The unwrapped phase images were subsequently combined into a single phase image via a weighted sum [19] over the two echoes, with weighting factor $\frac{TE_{1/2} \cdot e^{-TE_{1/2}/T_2^*}}{\sum_{n=1}^{2} TE_n \cdot e^{-TE_n/T_2^*}}$ [19] (T_2^* was set as 40 ms for all subjects). This effectively weights each echo by its predicted signal-to-noise ratio, enabling both echoes to contribute and thus boosting the signal-to-noise ratio of the final χ map.

The echo-combined phase image was then filtered to remove the background field contributions. Our pipeline uses the variable-kernel sophisticated harmonic artifact reduction for phase data (V-SHARP) algorithm [20] in the STI Suite toolbox with a maximum kernel size of 12 mm. The phase reliability and hole-filling steps described above were repeated on the

brain mask generated by V-SHARP, excluding voxels (connected to the sinus cavities) that had phase reliability values lower than 0.7 for the first echo or 0.6 for the second echo. The χ map was generated from the V-SHARP filtered phase data within this refined brain mask. Dipole inversion was performed using the iLSQR algorithm [21] in the STI Suite toolbox.

The final step is to calculate a reference χ value for each subject that will be subtracted from the output χ maps. As described above, we used the χ of CSF in the lateral ventricles as our reference. The χ map was transformed to subject's native T1 space where the UK Biobank pipeline has defined a ventricle mask in the BIANCA processing [12,97]. Inspection of the χ distribution in the ventricle mask (eroded by a 1mm radius spherical kernel) found that it contained a bimodal (Gaussian plus inverse gamma) distribution of χ estimates (**Supplementary Fig. S12**), which likely correspond to CSF and choroid plexus. To extract the CSF component of this distribution, we used an in-house mixture modelling algorithm [98]. The mean value of the central Gaussian distribution was considered to represent CSF voxels, and is used as the χ reference. The χ map in the original swMRI space was referenced to CSF by subtracting this reference value.

Image-derived phenotypes generation

In this study, QSM-based image-derived phenotypes (IDPs) were generated in 8 subcortical structures (thalamus, caudate, putamen, pallidum, hippocampus, amygdala, accumbens and substantia nigra) for both left and right (16 subcortical IDPs in total) and in white matter hyperintensity lesions (1 IDP in total). Masks for each subcortical structure in T1 space (excluding the substantia nigra) have been previously generated using FIRST (FMRIB's Integrated Registration and Segmentation Tool) [99] as part of the UK Biobank image processing pipeline. Masks for the substantia nigra used in this study were derived from a substantia nigra atlas [100] in MNI152 space. Masks for white matter, and white matter hyperintensity (WMH) lesions (derived from the BIANCA processing [12,97]) were provided to us in T1 space from the UK Biobank image processing pipeline. Masks for white matter generated using FAST (FMRIB's Automated Segmentation Tool) [101] were also provided to us in T1 space from the UK Biobank image processing pipeline. CSF referenced χ maps were transformed to both subject's native T1 space and MNI152 space, using the provided transformations from UK Biobank [12].

FIRST-generated subcortical masks were eroded (by a 2D 3x3 kernel) and then used to extract subcortical regions on CSF-referenced χ maps in the T1 space of each subject. The median χ-value (across extracted voxels) was calculated as a separate IDP for each of the left/right subcortical regions. The substantia nigra mask was used to extract the substantia nigra region on CSF referenced χ maps in the MNI152 space of each subject. To account for the morphological variations of substantia nigra across subjects, the substantia nigra mask was refined by excluding voxels that had negative χ values, with median χ values subsequently calculated as a separate IDP for left and right substantia nigra.

For the WMH IDP, the WMH mask was first used to extract the mean χ value in lesions. We then extracted the χ value from normal-appearing white matter, defined as the intersection of FAST- and BIANCA-based white matter mask with the WMH voxels removed. The difference between the estimated χ values of WMH and normal white matter was calculated as an IDP. This approach aims to isolate χ properties that are unique to lesions, as opposed to more global properties of white matter χ.

While most of the QSM IDPs use the same spatial ROIs as existing T2* IDPs, the previous pipelines did not include T2* of substantia nigra or WMH. We thus generated three new T2* IDPs for (substantia nigra left and right, and WMH). This enabled a direct comparison between QSM and T2* for 17 IDPs.

Outliers and confounds removal

Each IDP's $N_{subjects} \times 1$ vector first had outliers removed. Outliers were defined as being greater than 6x the median absolute deviation from the median. The remaining distribution of IDPs was then quantile normalised, resulting in it being Gaussian-distributed with mean zero and standard deviation one.

A recently expanded set of imaging confounds have been proposed in UK Biobank brain imaging [12,102] including age, head size, sex, head motion, scanner table position, imaging centre and scan-date-related slow drifts. Unless stated otherwise, the full set of imaging confounds were regressed out from the quantile normalised IDPs before any further analyses. This is crucial to avoid biased or spurious associations between IDPs and other non-imaging measures [11,102].

As reported in the literature, T2* estimates are biased by the presence of macroscopic field gradients (for example, induced by air/tissue interface), particularly when imaging voxels are large (in our case, using thick slices) [24]. To reduce such confounding effects on association analyses with UK Biobank T2* IDPs, we first modelled the relationship between macroscopic field gradients and R2* (1/T2*) measurement errors using both simulated and UK Biobank data [24]. This produced a macroscopic field gradient confound variable specific to each subject and brain region, which was generated and regressed out from T2* IDPs. No association was found between the field gradient confounds and QSM IDPs as expected, and thus this particular confound was only applied to T2* data. Details of this additional deconfounding for T2* IDPs are described in the Supplementary Material (Section 2).

We also observed strong negative correlations between QSM/T2* WMH IDPs and the WMH volume IDP provided by UK Biobank (**Fig. 1d**). This may indicate partial volume effects on the χ and T2* estimates within lesions. Thus, two sets of association analyses were carried out for QSM and T2* WMH IDPs with and without regressing out the WMH volume IDP.

Associations between IDPs and non-imaging measures

We utilised 17,485 non-imaging phenotypes (which are referred to here as phenotypes, as distinct from IDPs) from UK Biobank. Each of the 17,485 phenotypes used here had data from at least 40 subjects. The phenotypes spanned 17 groups of variable types, including early life factors (such as maternal smoking around birth), lifestyle factors (such as diet, alcohol and tobacco consumption), physical body measures (such as BMI, bone density and blood assays), cognitive test scores, health outcomes (such as clinical diagnosis – ICD10 and operative procedures – OPCS4) and mental health variables (such as bipolar and major depression status). These variables were automatically curated using the FUNPACK (the FMRIB UKBiobank Normalisation, Parsing And Cleaning Kit) software to ensure that all phenotypes variables (both quantitative and categorical) were numeric vectors and that resulting correlation coefficients were easy to interpret.

To investigate pairwise associations between IDPs and phenotypes, univariate statistics were carried out using Pearson correlation across all QSM/T2* measures (including 16 subcortical IDPs and 1 WMH IDP with/without regressing out WMH volume) and 17,485 phenotypes (quantile normalised and fully deconfounded). As UK Biobank phenotypes have varying amounts of missing data, the full set of associations of phenotypes against IDPs had widely-varying degrees-of-freedom. Therefore, it is important to consider P values (and not just correlation r); P values were calculated and used to identify the strongest associations. Bonferroni multiple comparison correction across the full set of 297,245 (17,485 x 18) correlations was applied, resulting in a $-\log_{10}P_{uncorrected}$ threshold of 6.80 (for $P_{corrected} < 0.05$).

Associations between IDPs and genetic variants

We carried out genome-wide association studies (GWASs, univariate correlations) for all QSM and T2* IDPs (including 16 subcortical IDPs and 1 WMH IDP with/without regressing out WMH volume), following a previously-described approach [36,37]. This was performed using the Spring 2018 UK Biobank release of imputed genetic data. From all subjects with an available χ map, we selected a subset of 29,579 unrelated subjects with recent UK ancestry (to avoid confounding effects from population structure or complex cross-subject covariance). We divided this set into a discovery cohort of 19,720 subjects and a replication cohort of 9,859 subjects. We applied QC filtering to the genetic data including minor allele frequency (MAF) ≥ 0.01, imputation information score ≥ 0.3 and Hardy-Weinberg equilibrium P value $\geq 10^{-7}$, which resulted in a total of 17,103,079 genetic variants (which are primarily SNPs, single-nucleotide polymorphisms). IDPs had both imaging and genetic confounds regressed out as carried out in Elliott et al. [36], including the above-described imaging confounds and 40 population genetic principal components (supplied by UK Biobank). IDPs were normalized (resulting in zero mean and unit variance) after the original Gaussianisation and deconfounding. GWAS was performed using the BGENIE software (https://jmarchini.org/bgenie/) [103].

Manhattan plots for each of the GWASs were produced, plotting the $-\log_{10}P$ value for each genetic variant. The standard single-phenotype GWAS threshold ($-\log_{10}P = 7.5$) [36,37] as well as an additional Bonferroni multiple comparison (across IDPs) corrected threshold ($-\log_{10}P = 8.73$) are shown in the plots. Peak associations with $-\log_{10}P$ value exceeding 7.5 were extracted and annotated using a method described in Elliott et al. [36]. That is, in a region of high linkage disequilibrium (LD), we only report the genetic variant with the highest association with the IDP because the associations in the local region are most likely all due to a single genetic effect [36,37,103].

After performing the GWAS, we used Peaks software (https://github.com/wnfldchen/peaks) [37] to automatically generate clusters of peak associations for all IDPs as described in refs. [36,37]. A cluster is a set of IDP/variant pairs for which all variants are within a 0.25-cM distance of the IDP/variant pair with highest $-\log_{10}P$ value in the cluster. Additionally, we used FUMA https://fuma.ctglab.nl [40] to map genetic variants identified in peak associations to related genes and to identify eQTL and chromatin mappings/interactions for these variants.

Following the approach described previously [36], we examined the heritability (h^2) of each subcortical IDP using LD score regression (LDSC) [38] on all available subjects (combining discovery and reproduction cohorts). LD scores were sourced from the European population of the 1000 Genomes Project [104]. Due to limitations in 1000 Genome Project linkage disequilibrium score files, the X chromosome is not considered in this analysis.

Voxel-wise associations with phenotypes and genetic variants

The MNI152-space versions of CSF referenced χ maps from all subjects were also combined into a 4D MNI152 χ matrix (of size $182 \times 218 \times 182 \times N_{subjects}$). Each of the voxel vectors in the 4D MNI152 χ matrix had outliers removed and was quantile normalised and fully deconfounded.

We carried out voxel-wise correlations between the χ maps and non-imaging measures (both phenotypes and genetic variants) that had been identified to have significant associations with QSM-based IDPs. Interrogating χ maps at a voxel-wise level can provide further insight into the spatial localization of associations and can potentially identify additional associated areas which were not captured by the original IDPs, either because a given brain region was explicitly not included or because heterogeneity within a larger brain region diluted an association with a sub-region. Univariate Pearson correlations were performed between fully deconfounded χ data vectors (voxels across the 4D MNI152 χ matrix) and phenotypes or genetic variant data vectors, resulting in 3D correlation maps.

Acknowledgements

This research was conducted using the UK Biobank Resource under application number 8107. We are grateful to UK Biobank for making the data available and to all UK Biobank study participants, who generously donated their time to make this resource possible. The Wellcome Centre for Integrative Neuroimaging is supported by core funding from the Wellcome Trust (203139/Z/16/Z). **CW** is funded in part by the China Scholarship Council (CSC). **KM** is supported by a Wellcome Trust Senior Research Fellowship 202788/Z/16/Z. **SS** and **GD** are supported by a Wellcome Trust Collaborative Award 215573/Z/19/Z. **AL** is supported by the Horizon 2020 Programme CANDY (Grant No. 847818). Computation partially used the Oxford Biomedical Research Computing (BMRC) facility, a joint development between the Wellcome Centre for Human Genetics and the Big Data Institute supported by Health Data Research UK and the NIHR Oxford Biomedical Research Centre.

References

1. Lerch, J. P. *et al.* Studying neuroanatomy using MRI. *Nature Neuroscience* **20**, 314–326 (2017).
2. Haacke, E. M., Xu, Y., Cheng, Y.-C. N. & Reichenbach, J. R. Susceptibility weighted imaging (SWI). *Magnetic Resonance in Medicine* **52**, 612–618 (2004).
3. Duyn, J. MR susceptibility imaging. *Journal of Magnetic Resonance* **229**, 198–207 (2013).
4. Liu, C., Li, W., Tong, K. A., Yeom, K. W. & Kuzminski, S. Susceptibility-weighted imaging and quantitative susceptibility mapping in the brain. *Journal of Magnetic Resonance Imaging* **42**, 23–41 (2015).
5. Gong, N.-J., Dibb, R., Bulk, M., van der Weerd, L. & Liu, C. Imaging beta amyloid aggregation and iron accumulation in Alzheimer's disease using quantitative susceptibility mapping MRI. *NeuroImage* **191**, 176–185 (2019).
6. Du, G. *et al.* Distinct progression pattern of susceptibility MRI in the substantia nigra of Parkinson's patients. *Movement Disorders* **33**, 1423–1431 (2018).
7. Schweser, F. *et al.* Mapping of thalamic magnetic susceptibility in multiple sclerosis indicates decreasing iron with disease duration: A proposed mechanistic relationship between inflammation and oligodendrocyte vitality. *NeuroImage* **167**, 438–452 (2018).
8. Zivadinov, R. *et al.* Brain Iron at Quantitative MRI Is Associated with Disability in Multiple Sclerosis. *Radiology* **289**, 487–496 (2018).
9. Li, Y. *et al.* Iron Content in Deep Gray Matter as a Function of Age Using Quantitative Susceptibility Mapping: A Multicenter Study. *Frontiers in Neuroscience* **14**, 1389 (2021).
10. Littlejohns, T. J. *et al.* The UK Biobank imaging enhancement of 100,000 participants: rationale, data collection, management and future directions. *Nature Communications* **11**, 2624 (2020).
11. Miller, K. L. *et al.* Multimodal population brain imaging in the UK Biobank prospective epidemiological study. *Nature Neuroscience* **19**, 1523–1536 (2016).
12. Alfaro-Almagro, F. *et al.* Image processing and Quality Control for the first 10,000 brain imaging datasets from UK Biobank. *NeuroImage* **166**, 400–424 (2018).
13. Glasser, M. F. *et al.* The minimal preprocessing pipelines for the Human Connectome Project. *NeuroImage* **80**, 105–124 (2013).
14. Haacke, E. M. *et al.* Quantitative susceptibility mapping: Current status and future directions. *Magnetic Resonance Imaging* vol. 33 1–25 (2015).
15. Robinson, S. D. *et al.* An illustrated comparison of processing methods for MR phase imaging and QSM: combining array coil signals and phase unwrapping. *NMR in Biomedicine* **30**, e3601 (2017).
16. Schweser, F., Robinson, S. D., de Rochefort, L., Li, W. & Bredies, K. An illustrated comparison of processing methods for phase MRI and QSM: removal of background field contributions from sources outside the region of interest. *NMR in Biomedicine* **30**, e3604 (2017).
17. Eckstein, K. *et al.* Computationally Efficient Combination of Multi-channel Phase Data From Multi-echo Acquisitions (ASPIRE). *Magnetic Resonance in Medicine* **79**, 2996–3006 (2018).
18. Schofield, M. A. & Zhu, Y. Fast phase unwrapping algorithm for interferometric applications. *Opt. Lett.* **28**, 1194–1196 (2003).
19. Wu, B., Li, W., Avram, A. V., Gho, S. M. & Liu, C. Fast and tissue-optimized mapping of magnetic susceptibility and T2* with multi-echo and multi-shot spirals. *NeuroImage* **59**, 297–305 (2012).

20. Schweser, F., Deistung, A., Lehr, B. W. & Reichenbach, J. R. Quantitative imaging of intrinsic magnetic tissue properties using MRI signal phase: An approach to in vivo brain iron metabolism? *NeuroImage* **54**, 2789–2807 (2011).
21. Li, W. *et al.* A method for estimating and removing streaking artifacts in quantitative susceptibility mapping. *NeuroImage* **108**, 111–122 (2015).
22. Yablonskiy, D. A. & Haacke, E. M. Theory of NMR signal behavior in magnetically inhomogeneous tissues: The static dephasing regime. *Magnetic Resonance in Medicine* **32**, 749–763 (1994).
23. Wang, C. *et al.* Methods for quantitative susceptibility and R2* mapping in whole post-mortem brains at 7T applied to amyotrophic lateral sclerosis. *NeuroImage* **222**, 117216 (2020).
24. Hernando, D., Vigen, K. K., Shimakawa, A. & Reeder, S. B. R2* mapping in the presence of macroscopic B0 field variations. *Magnetic Resonance in Medicine* **68**, 830–840 (2012).
25. Jolobe, O. M. P. Mean corpuscular haemoglobin, referenced and resurrected. *Journal of Clinical Pathology* **64**, 833 (2011).
26. Langkammer, C. *et al.* Quantitative susceptibility mapping (QSM) as a means to measure brain iron? A post mortem validation study. *NeuroImage* **62**, 1593–1599 (2012).
27. Chaturvedi, R. K. *et al.* Neuroprotective and neurorescue effect of black tea extract in 6-hydroxydopamine-lesioned rat model of Parkinson's disease. *Neurobiology of Disease* **22**, 421–434 (2006).
28. Mandel, S., Amit, T., Reznichenko, L., Weinreb, O. & Youdim, M. B. H. Green tea catechins as brain-permeable, natural iron chelators-antioxidants for the treatment of neurodegenerative disorders. *Molecular Nutrition & Food Research* **50**, 229–234 (2006).
29. Schweser, F. *et al.* Decreasing brain iron in multiple sclerosis: The difference between concentration and content in iron MRI. *Human Brain Mapping* **42**, 1463–1474 (2021).
30. Swaminathan, S., Fonseca, V. A., Alam, M. G. & Shah, S. v. The Role of Iron in Diabetes and Its Complications. *Diabetes Care* **30**, 1926 (2007).
31. Li, J., Zhang, Q., Zhang, N. & Guo, L. Increased Brain Iron Detection by Voxel-Based Quantitative Susceptibility Mapping in Type 2 Diabetes Mellitus Patients With an Executive Function Decline. *Frontiers in Neuroscience* **14**, 1390 (2021).
32. Juhás, M. *et al.* Deep grey matter iron accumulation in alcohol use disorder. *NeuroImage* **148**, 115–122 (2017).
33. Pitel, A. L., Segobin, S. H., Ritz, L., Eustache, F. & Beaunieux, H. Thalamic abnormalities are a cardinal feature of alcohol-related brain dysfunction. *Neuroscience and Biobehavioral Reviews* **54**, 38–45 (2015).
34. Segobin, S. *et al.* Dissociating thalamic alterations in alcohol use disorder defines specificity of Korsakoff's syndrome. *Brain* **142**, 1458–1470 (2019).
35. Prins, N. D. & Scheltens, P. White matter hyperintensities, cognitive impairment and dementia: an update. *Nature Reviews Neurology* **11**, 157–165 (2015).
36. Elliott, L. T. *et al.* Genome-wide association studies of brain imaging phenotypes in UK Biobank. *Nature* **562**, 210–216 (2018).
37. Smith, S. M. *et al.* An expanded set of genome-wide association studies of brain imaging phenotypes in UK Biobank. *Nature Neuroscience* **24**, 737–745 (2021).
38. Bulik-Sullivan, B. K. *et al.* LD Score regression distinguishes confounding from polygenicity in genome-wide association studies. *Nature Genetics* **47**, 291–295 (2015).
39. Yang, J. *et al.* Common SNPs explain a large proportion of the heritability for human height. *Nature Genetics* **42**, 565–569 (2010).

40. Watanabe, K., Taskesen, E., van Bochoven, A. & Posthuma, D. Functional mapping and annotation of genetic associations with FUMA. *Nature Communications* **8**, 1826 (2017).
41. Anderson, G. J. & Bardou-Jacquet, E. Revisiting hemochromatosis: genetic vs. phenotypic manifestations. *Annals of Translational Medicine* **9**, (2021).
42. Benyamin, B. *et al.* Variants in TF and HFE Explain ~40% of Genetic Variation in Serum-Transferrin Levels. *American Journal of Human Genetics* **84**, 60–65 (2009).
43. Raffield, L. M. *et al.* Genome-wide association study of iron traits and relation to diabetes in the Hispanic Community Health Study/Study of Latinos (HCHS/SOL): potential genomic intersection of iron and glucose regulation? *Human Molecular Genetics* **26**, 1966–1978 (2017).
44. Kauwe, J. S. K. *et al.* Suggestive synergy between genetic variants in TF and HFE as risk factors for Alzheimer's disease. *American Journal of Medical Genetics Part B: Neuropsychiatric Genetics* **153B**, 955–959 (2010).
45. Ma, L., Tian, Y., Peng, C., Zhang, Y. & Zhang, S. Recent advances in the epidemiology and genetics of acute intermittent porphyria. *Intractable & Rare Diseases Research* **advpub**, (2020).
46. Kevelam, S. H. *et al.* Acute intermittent porphyria-related leukoencephalopathy. *Neurology* **87**, 1258 (2016).
47. Park, J. H. *et al.* SLC39A8 Deficiency: A Disorder of Manganese Transport and Glycosylation. *American Journal of Human Genetics* **97**, 894–903 (2015).
48. Boycott, K. M. *et al.* Autosomal-Recessive Intellectual Disability with Cerebellar Atrophy Syndrome Caused by Mutation of the Manganese and Zinc Transporter Gene SLC39A8. *American Journal of Human Genetics* **97**, 886–893 (2015).
49. Ehret, G. B. *et al.* Genetic variants in novel pathways influence blood pressure and cardiovascular disease risk. *Nature* **478**, 103–109 (2011).
50. Lind, L. Genome-Wide Association Study of the Metabolic Syndrome in UK Biobank. *Metabolic Syndrome and Related Disorders* **17**, 505–511 (2019).
51. Carrera, N. *et al.* Association study of nonsynonymous single nucleotide polymorphisms in schizophrenia. *Biological Psychiatry* **71**, 169–177 (2012).
52. Smeland, O. B. *et al.* Genome-wide Association Analysis of Parkinson's Disease and Schizophrenia Reveals Shared Genetic Architecture and Identifies Novel Risk Loci. *Biological Psychiatry* **89**, 227–235 (2021).
53. Thompson, A. *et al.* Functional validity, role, and implications of heavy alcohol consumption genetic loci. *Science Advances* **6**, eaay5034 (2020).
54. Chen, M. H. *et al.* Trans-ethnic and Ancestry-Specific Blood-Cell Genetics in 746,667 Individuals from 5 Global Populations. *Cell* **182**, 1198-1213.e14 (2020).
55. Luo, Q. *et al.* Association of a Schizophrenia-Risk Nonsynonymous Variant With Putamen Volume in Adolescents: A Voxelwise and Genome-Wide Association Study. *JAMA Psychiatry* **76**, 435–445 (2019).
56. Zhao, B. *et al.* Large-scale GWAS reveals genetic architecture of brain white matter microstructure and genetic overlap with cognitive and mental health traits (n = 17,706). *Molecular Psychiatry* (2019) doi:10.1038/s41380-019-0569-z.
57. Chowanadisai, W., Graham, D. M., Keen, C. L., Rucker, R. B. & Messerli, M. A. Neurulation and neurite extension require the zinc transporter ZIP12 (*slc39a12*). *Proceedings of the National Academy of Sciences* **110**, 9903 (2013).
58. Buraei, Z. & Yang, J. The β Subunit of Voltage-Gated Ca2+ Channels. *Physiological Reviews* **90**, 1461–1506 (2010).

59. Green, E. K. *et al.* The bipolar disorder risk allele at CACNA1C also confers risk of recurrent major depression and of schizophrenia. *Molecular Psychiatry* **15**, 1016–1022 (2010).
60. Liao, X. & Li, Y. Genetic associations between voltage-gated calcium channels and autism spectrum disorder: a systematic review. *Molecular Brain* **13**, 96 (2020).
61. Smoller, J. W. *et al.* Identification of risk loci with shared effects on five major psychiatric disorders: A genome-wide analysis. *The Lancet* **381**, 1371–1379 (2013).
62. Calcraft, P. J. *et al.* NAADP mobilizes calcium from acidic organelles through two-pore channels. *Nature* **459**, 596–600 (2009).
63. Fernández, B. *et al.* Iron overload causes endolysosomal deficits modulated by NAADP-regulated 2-pore channels and RAB7A. *Autophagy* **12**, 1487–1506 (2016).
64. Ziegler, D. v *et al.* Calcium channel ITPR2 and mitochondria–ER contacts promote cellular senescence and aging. *Nature Communications* **12**, 720 (2021).
65. Blokland, G. A. M. *et al.* Genome-wide association study of working memory brain activation. *International Journal of Psychophysiology* **115**, 98–111 (2017).
66. Brenner, M. *et al.* Mutations in GFAP, encoding glial fibrillary acidic protein, are associated with Alexander disease. *Nature Genetics* **27**, 117–120 (2001).
67. Bettcher, B. M. *et al.* Astrogliosis and episodic memory in late life: higher GFAP is related to worse memory and white matter microstructure in healthy aging and Alzheimer's disease. *Neurobiology of Aging* **103**, 68–77 (2021).
68. Bellaver, B. *et al.* Astrocyte Biomarkers in Alzheimer Disease. *Neurology* **96**, e2944 (2021).
69. Goursaud, S., Kozlova, E. N., Maloteaux, J.-M. & Hermans, E. Cultured astrocytes derived from corpus callosum or cortical grey matter show distinct glutamate handling properties. *Journal of Neurochemistry* **108**, 1442–1452 (2009).
70. Islam, S. & Watanabe, H. Versican: A Dynamic Regulator of the Extracellular Matrix. *Journal of Histochemistry & Cytochemistry* **68**, 763–775 (2020).
71. Wight, T. N., Kang, I. & Merrilees, M. J. Versican and the control of inflammation. *Matrix Biology* **35**, 152–161 (2014).
72. Sobel, R. A. The extracellular matrix in multiple sclerosis: an update. *Brazilian Journal of Medical and Biological Research* **34**, (2001).
73. de Jong, J. M., Wang, P., Oomkens, M. & Baron, W. Remodeling of the interstitial extracellular matrix in white matter multiple sclerosis lesions: Implications for remyelination (failure). *Journal of Neuroscience Research* **98**, 1370–1397 (2020).
74. Rutten-Jacobs, L. C. A. *et al.* Genetic Study of White Matter Integrity in UK Biobank (N=8448) and the Overlap With Stroke, Depression, and Dementia. *Stroke* **49**, 1340–1347 (2018).
75. Argyridis, I., Li, W., Johnson, G. A. & Liu, C. Quantitative magnetic susceptibility of the developing mouse brain reveals microstructural changes in the white matter. *NeuroImage* **88**, 134–142 (2014).
76. Oshima, S. *et al.* Brain MRI with Quantitative Susceptibility Mapping: Relationship to CT Attenuation Values. *Radiology* **294**, 600–609 (2020).
77. Ramos, P. *et al.* Iron levels in the human brain: A post-mortem study of anatomical region differences and age-related changes. *Journal of Trace Elements in Medicine and Biology* **28**, 13–17 (2014).
78. Andrási, E., Igaz, S., Szoboszlai, N., Farkas, É. & Ajtony, Z. Several methods to determine heavy metals in the human brain. *Spectrochimica acta, Part B: Atomic spectroscopy* **54**, 819–825 (1999).
79. Hibar, D. P. *et al.* Common genetic variants influence human subcortical brain structures. *Nature* **520**, 224–229 (2015).

80. Allen, N. *et al.* UK Biobank: Current status and what it means for epidemiology. *Health Policy and Technology* **1**, 123–126 (2012).
81. Eshaghi, A. *et al.* Identifying multiple sclerosis subtypes using unsupervised machine learning and MRI data. *Nature Communications* **12**, 2078 (2021).
82. Nobis, L. *et al.* Hippocampal volume across age: Nomograms derived from over 19,700 people in UK Biobank. *NeuroImage: Clinical* **23**, 101904 (2019).
83. Raman, B. *et al.* Medium-term effects of SARS-CoV-2 infection on multiple vital organs, exercise capacity, cognition, quality of life and mental health, post-hospital discharge. *EClinicalMedicine* **31**, 100683 (2021).
84. Rouault, T. A. Iron metabolism in the CNS: implications for neurodegenerative diseases. *Nature Reviews Neuroscience* **14**, 551–564 (2013).
85. Ward, R. J., Zucca, F. A., Duyn, J. H., Crichton, R. R. & Zecca, L. The role of iron in brain ageing and neurodegenerative disorders. *The Lancet Neurology* vol. 13 1045–1060 (2014).
86. Marambaud, P., Dreses-Werringloer, U. & Vingtdeux, V. Calcium signaling in neurodegeneration. *Molecular Neurodegeneration* **4**, 20 (2009).
87. Pchitskaya, E., Popugaeva, E. & Bezprozvanny, I. Calcium signaling and molecular mechanisms underlying neurodegenerative diseases. *Cell Calcium* vol. 70 87–94 (2018).
88. Liu, C. *et al.* Quantitative Susceptibility Mapping: Contrast Mechanisms and Clinical Applications. *Tomography* **1**, (2015).
89. Wang, Y. & Liu, T. Quantitative susceptibility mapping (QSM): Decoding MRI data for a tissue magnetic biomarker. *Magnetic Resonance in Medicine* **73**, 82–101 (2015).
90. Liu, T. *et al.* A novel background field removal method for MRI using projection onto dipole fields (PDF). *NMR in Biomedicine* **24**, 1129–1136 (2011).
91. Zhou, D., Liu, T., Spincemaille, P. & Wang, Y. Background field removal by solving the Laplacian boundary value problem. *NMR in Biomedicine* **27**, 312–319 (2014).
92. Liu, J. *et al.* Morphology enabled dipole inversion for quantitative susceptibility mapping using structural consistency between the magnitude image and the susceptibility map. *NeuroImage* **59**, 2560–2568 (2012).
93. Wei, H. *et al.* Streaking artifact reduction for quantitative susceptibility mapping of sources with large dynamic range. *NMR in Biomedicine* **28**, 1294–1303 (2015).
94. Zhang, L. *et al.* Fast quantitative susceptibility reconstruction via total field inversion with improved weighted L0 norm approximation. *NMR in Biomedicine* **32**, e4067 (2019).
95. Deistung, A. *et al.* Toward in vivo histology: A comparison of quantitative susceptibility mapping (QSM) with magnitude-, phase-, and R2*-imaging at ultra-high magnetic field strength. *NeuroImage* **65**, 299–314 (2013).
96. Jenkinson, M. Fast, automated, N-dimensional phase-unwrapping algorithm. *Magnetic Resonance in Medicine* **49**, 193–197 (2003).
97. Griffanti, L. *et al.* BIANCA (Brain Intensity AbNormality Classification Algorithm): A new tool for automated segmentation of white matter hyperintensities. *NeuroImage* **141**, 191–205 (2016).
98. Llera, A., Vidaurre, D., Pruim, R. H. R. & Beckmann, C. F. Variational Mixture Models with Gamma or inverse-Gamma components. (2016).
99. Patenaude, B., Smith, S. M., Kennedy, D. N. & Jenkinson, M. A Bayesian model of shape and appearance for subcortical brain segmentation. *NeuroImage* **56**, 907–922 (2011).
100. Pauli, W. M., Nili, A. N. & Tyszka, J. M. A high-resolution probabilistic in vivo atlas of human subcortical brain nuclei. *Scientific Data* **5**, 180063 (2018).

101. Zhang, Y., Brady, M. & Smith, S. Segmentation of brain MR images through a hidden Markov random field model and the expectation-maximization algorithm. *IEEE Transactions on Medical Imaging* **20**, (2001).
102. Alfaro-Almagro, F. *et al.* Confound modelling in UK Biobank brain imaging. *NeuroImage* **224**, 117002 (2021).
103. Bycroft, C. *et al.* The UK Biobank resource with deep phenotyping and genomic data. *Nature* **562**, 203–209 (2018).
104. Auton, A. *et al.* A global reference for human genetic variation. *Nature* **526**, 68–74 (2015).